RSC Advances

PAPER

View Article Online
View Journal | View Issue



Cite this: *RSC Adv.*, 2026, **16**, 21201

# Mitigating heavy metals leachability from $CO_2$ carbonated coal-based solid waste backfill in high-salinity environments *via* biochar-clay-nanomaterial synergistic modification

Zhishang Zhang,[abcd] Liqiang Ma,*[abcd] Ichhuy Ngo,*[a] Kunpeng Yu,[a] Jiangtao Zhai,[a] Zezhou Guo,[a] Zhiyang Zhao,[a] Chengkun Peng[a] and Ruizhi Yang[a]

High-salinity mine water exerts an uncertain influence on the leaching behavior of heavy metals in $CO_2$-carbonated backfill material (CCB), posing potential environmental risks. To address this, this study develops a novel CCB using locally sourced solid waste and high-salinity mine water from a certain mining area, and proposes a control strategy involving rice husk biochar (RHB), natural clinoptilolite (NCP), sepiolite (SEP), and γ-phase nano-$Al_2O_3$ (NA) as a synergistic modifier. Through static and dynamic leaching tests, combined with ICP-MS, SEM, XRD, and FTIR analysis, this study investigates the leaching behavior of heavy metals before and after modification, while evaluating the mechanical properties and other parameters to assess the engineering applicability of the modified CCB. The results indicated that high-salinity environments (rich in $SO_4^{2-}$ and $Cl^-$) promoted the expansion and cracking of CCB, increasing the risk of heavy metals leaching. However, the introduction of the modifiers effectively suppressed the leaching of Cr, Ni, Mn, and other heavy metals through mechanisms such as electrostatic attraction, precipitation, ion exchange and complexation. Among the single-modifier systems, SEP demonstrated the most significant effect, reducing the average leaching of heavy metals by approximately 75.78%, though limitations remained for elements like Cr. The synergistic modification system ensures all detected heavy metals concentrations are below the Class IV groundwater quality standard (based on TCLP results), while enhancing porosity and adsorption capacity without sacrificing mechanical properties. The addition of NA enhanced mechanical strength but its effectiveness in controlling heavy metals leaching varied depending on the accompanying modifiers.

Received 22nd December 2025
Accepted 16th April 2026

DOI: 10.1039/d5ra09892k

rsc.li/rsc-advances



## 1. Introduction

Coal-fired power generation, blast furnace ironmaking, and other industrial processes produce large amounts of solid waste, such as fly ash (FA) and blast furnace slag (SG).[1] Given the pozzolanic potential of these waste materials, some researchers have suggested using them as substitutes for cement to produce backfill materials that can address surface subsidence issues caused by coal mining, while also reducing the high carbon emissions associated with cement production.[2] Additionally, the disposal of power plant flue gases, represented by $CO_2$ emissions, is also a pressing concern.[3] As the carbon neutrality strategy progresses, attention has turned to the feasibility of using cementitious backfill materials to create an alkaline environment for capturing and storing $CO_2$, such as the preparation of $CO_2$ carbonated coal-based solid waste backfill (CCB).[4] However, the use of such backfill materials faces limitations due to locally sourced raw materials (such as solid waste, flue gases, and mine water), resulting in significant uncertainty regarding their physicochemical properties and stability. This makes it challenging to accurately assess their potential environmental impact. In terms of raw materials, both FA and SG are solid waste products of high-temperature pyrolysis processes and generally present a high risk of heavy metals leaching (*e.g.*, Cr, Ni, Cu).[5] Notably, the leaching behavior of heavy metals from different coal types varies significantly after high-temperature pyrolysis. Since these heavy metal pollutants are difficult to degrade in the natural environment, they may migrate and accumulate through water cycles and the food chain, ultimately entering the human body. Long-term accumulation could pose health risks, including carcinogenesis or respiratory system damage.[6]

[a]*School of Mines, China University of Mining and Technology, Xuzhou, 221116, China. E-mail: 4225@cumt.edu.cn; ngoichhuy@cumt.edu.cn*

[b]*Xinjiang Key Laboratory of Coal-bearing Resources Exploration and Exploitation, Xinjiang Institute of Engineering, Urumqi, 830023, China*

[c]*Xinjiang Engineering Research Center of Green Intelligent Coal Mining, Xinjiang Institute of Engineering, Urumqi, 830023, China*

[d]*Key Laboratory of Xinjiang Coal Resources Green Mining (Xinjiang Institute of Engineering), Ministry of Education, Urumqi, 830023, China*

Prior to this study, a significant amount of research has been conducted on the environmental stability of backfill materials before $CO_2$ carbonation. For instance, Yang *et al.*[7] employed the horizontal vibration method to investigate the leachability of heavy metals from magnesium-coal slag solid waste backfill materials, finding that the hardening of the slurry effectively controlled the leaching to levels below the Class III groundwater quality standard. However, in a study of similar coal-based solid waste backfills, Long *et al.*[8] discovered that the leaching of Ni exceeded the Class III standard limit. Their findings also suggested that pH played a critical role in the leaching of heavy metals. Additionally, Hu *et al.*[9] studied the leaching behavior of coal fly ash-based geopolymers and found that although the geopolymer effectively immobilized heavy metals such as Fe, Cr, As, Cd, and Ti in FA, its control over Mn and Ni was limited. These results indicate that for cementitious backfill systems, differences in raw materials, reaction conditions, and even testing methods can lead to significant variations in the leaching behavior of heavy metals. Building on this, the introduction of coal-fired flue gases, represented by $CO_2$, is likely to reduce the overall pH of the reaction system,[10] increasing the uncertainty of heavy metals leaching from the CCB. Furthermore, in major mining areas in northwestern China, particularly in Xinjiang, the salinity of mine water is exceptionally high, with mineralization levels often exceeding 5000 mg $L^{-1}$ and reaching up to 10 000 mg $L^{-1}$ in some regions, classifying it as high-salinity mine water.[11] Whether the continuous exposure of backfill materials to high-salinity mine water will exacerbate or mitigate the leaching risk of heavy metals requires further investigation.

Currently, traditional methods for controlling heavy metals leaching from solid waste mainly rely on chemical stabilizers or physical coating technologies, such as direct precipitation.[12–14] However, these methods not only have limited control effectiveness but may also pose new environmental risks.[15] Particularly in high-salinity environments, the effectiveness of heavy metals fixation relying on precipitation is easily disturbed, leading to reduced stability efficiency. In contrast, porous materials, such as biochar and clay, have shown great potential in the field of heavy metals immobilization due to their excellent adsorption properties, ion exchange capacity, and structural stability.[16] Biochar, a carbon-rich solid produced by the anaerobic pyrolysis of plant biomass, is particularly effective in adsorbing and immobilizing heavy metals due to its rich functional groups and porous structure. However, its high carbon content may suppress the expression of pozzolanic activity, thus hindering the improvement of backfill strength.[17] This contradiction limits its widespread use in cementitious backfill materials. Notably, the pozzolanic activity of biochar is closely related to its raw material. For example, Liu *et al.*[18] found that bamboo-derived biochar exhibited poor pozzolanic reactivity, while Chen *et al.*[19] reported that rice husk biochar, even with a high fixed carbon content, still demonstrated pozzolanic activity. Moreover, rice husk biochar is abundantly available, with an estimated global annual production of 28 million tons, making it a promising material for application.[20] Clay materials are another class of widely studied adsorbents.[21] Natural zeolites, such as clinoptilolite, are abundant and inexpensive, with their regular pore structure and exchangeable cations (*e.g.*, $Na^+$, $K^+$, $Ca^{2+}$) providing excellent ion adsorption and exchange capacity. Studies show that their adsorption performance and structural stability are closely related to the Si/Al ratio.[22] A lower Si/Al ratio typically corresponds to higher adsorption capacity but poorer structural stability, while a higher Si/Al ratio improves stability but may result in some loss of adsorption capacity, making it difficult to balance both properties. Furthermore, sepiolite ($Mg_4[Si_6O_{15}](OH)_2 \cdot 3H_3O$), a fibrous hydrated magnesium silicate, has also been widely studied for its adsorption capacity. Unlike the regular pore structure of natural clinoptilolite, sepiolite has a layered structure where interlayer cations and water molecules can participate in ion exchange. Its surface is also rich in hydroxyl functional groups, which contribute to its strong adsorption ability.[23]

It is important to note that the introduction of porous materials often alters the pore structure and pore size distribution of the backfill, which can lead to a decrease in mechanical strength and overall stability.[24] This degradation compromises the structural integrity and long-term durability of the backfill, thus limiting the widespread application of porous materials in backfill modification. Studies have shown that nanoparticles, due to their nanoscale particle size and extremely high specific surface area, exhibit significant nano-filling, bridging, and nucleation effects,[25] which may help to compensate for the structural deficiencies of porous materials. Among various nanoparticles, nano-$Al_2O_3$ has attracted significant attention in the field of cement-based material modification due to its high stability and excellent mechanical properties.[26] However, its pore-filling behavior may reduce the availability of active sites, thus weakening its adsorption capacity for heavy metals and limiting its applicability. It is also important to distinguish that the performance of nanoparticles is closely related to their crystalline structure. Compared to $\alpha$ and $\delta$ phases, $\gamma$-phase nano-$Al_2O_3$ has a higher specific surface area and more abundant surface active sites due to its loose and porous mesoporous structure.[27,28] This suggests that $\gamma$-phase nano-$Al_2O_3$ may not only maintain the mechanical strength and structural stability of the backfill but also retain excellent adsorption properties for heavy metals.

Therefore, this study aims to take the Hami Dananhu No. 1 Mine in Xinjiang as a case study. By using locally sourced materials—fly ash, slag, and high-salinity mine water, the study will employ $CO_2$ carbonation technology to prepare $CO_2$ carbonated coal-based solid waste backfill (CCB) and systematically evaluate their heavy metals leaching behavior. On this basis, the study will explore the control effects of synergistic modifiers, including rice husk biochar, natural clinoptilolite, sepiolite, and $\gamma$-phase nano-$Al_2O_3$, on the leaching behavior of the CCB. Additionally, the mechanical properties and long-term stability of the modified backfill will be comprehensively assessed to evaluate its engineering applicability. This research will provide a theoretical basis and research methodology for controlling heavy metals pollution and promoting the resource utilization of solid waste in $CO_2$ carbonated coal-based solid waste backfill under high-salinity mine water conditions.

## 2. Materials and methods

### 2.1. Materials

**2.1.1. Fly ash, slag and modifiers.** The raw materials consists of FA and SG, supplied by Dananhu Power Plant of State Grid Energy Hami Coal Power Co., Ltd. The modifiers are composed of biochar, zeolite, sepiolite, and nanomaterials. Biochar is derived from rice husk biochar (RHB), pyrolyzed at 600 °C. Fresh rice husks were air-dried, then placed in a muffle furnace and heated to 600 °C under anaerobic conditions. Then the ash was cleaned with deionized water (DW) and anhydrous ethanol, dried, ground and sieved through a 150-mesh sieve. The zeolite powder is Na-type natural clinoptilolite (NCP), provided by Henan Bangneng Metal Materials Co., Ltd. Sepiolite (SEP) is a hydrothermal low-calcium sepiolite, provided by Guzhang County Shanlin Shiyu Mining Products Co., Ltd. The nanomaterial is γ-phase nano-$Al_2O_3$ particles (NA) with 99.99% purity and an average particle size of 40 nm, supplied by Hangzhou Jigong Biotechnology Co., Ltd.

To further investigate the fundamental properties of the raw materials and modifiers, X-ray diffractometry (XRD, Puxi General XD-6), laser particle size analysis (PSA, Malvern Mastersizer 3000), and field emission scanning electron microscopy (SEM, ZEISS Sigma 300) were used to analyze the phase composition, particle size distribution, and microstructure of them, respectively. All test results are presented in Fig. 1. Additionally, the specific surface area, total pore volume, and average pore diameter were measured by an automated specific surface area and porosity analyzer (BET, Micromeritics ASAP 2460) (The $N_2$ adsorption–desorption isotherms are shown in SI Fig. S1). The oxide composition of the material was determined *via* X-ray fluorescence spectroscopy (XRF, Rigaku ZSX Primus III+). The XRF results, together with the materials' basic characteristics including morphology, mesoporous structure, and particle size, are summarized in Table 1.

The results indicate that the phase composition of FA primarily consists of mullite, quartz, and a small amount of hematite, which is consistent with the higher contents of $Al_2O_3$, $SiO_2$, and $Fe_2O_3$ observed in the XRF analysis. SG mainly consists of quartz, calcite, and dicalcium silicate ($C_2S$), and a typical broad diffraction peak is observed around $2\theta = 30°$, suggesting the presence of a large amount of amorphous glassy phase. Its oxides are predominantly CaO, $SiO_2$, $Al_2O_3$, and a small amount of MgO. The main structure of RHB is amorphous, with only the crystal diffraction peak corresponding to quartz observed around 44°, indicating the presence of crystalline $SiO_2$. The main phases of NCP, SEP, and NA correspond to clinoptilolite, sepiolite, and γ-$Al_2O_3$, respectively, while the other small peaks are attributed to quartz and calcite. XRF results show that NCP is rich in $SiO_2$ and $Al_2O_3$, while SEP is mainly composed of $SiO_2$ and MgO. The particle size distribution follows the trend of RHB > SEP > NCP > FA > SG, with SG having the finest particle size, where D90 is only 28.10 μm, and NCP also contains a considerable amount of smaller particles. In terms of microstructure, FA exhibits typical spherical particles, and NA is also spherical. SG and NCP mainly exhibit blocky or laminar structures, while SEP presents a clear fibrous morphology. The RHB particles are relatively larger, with a large

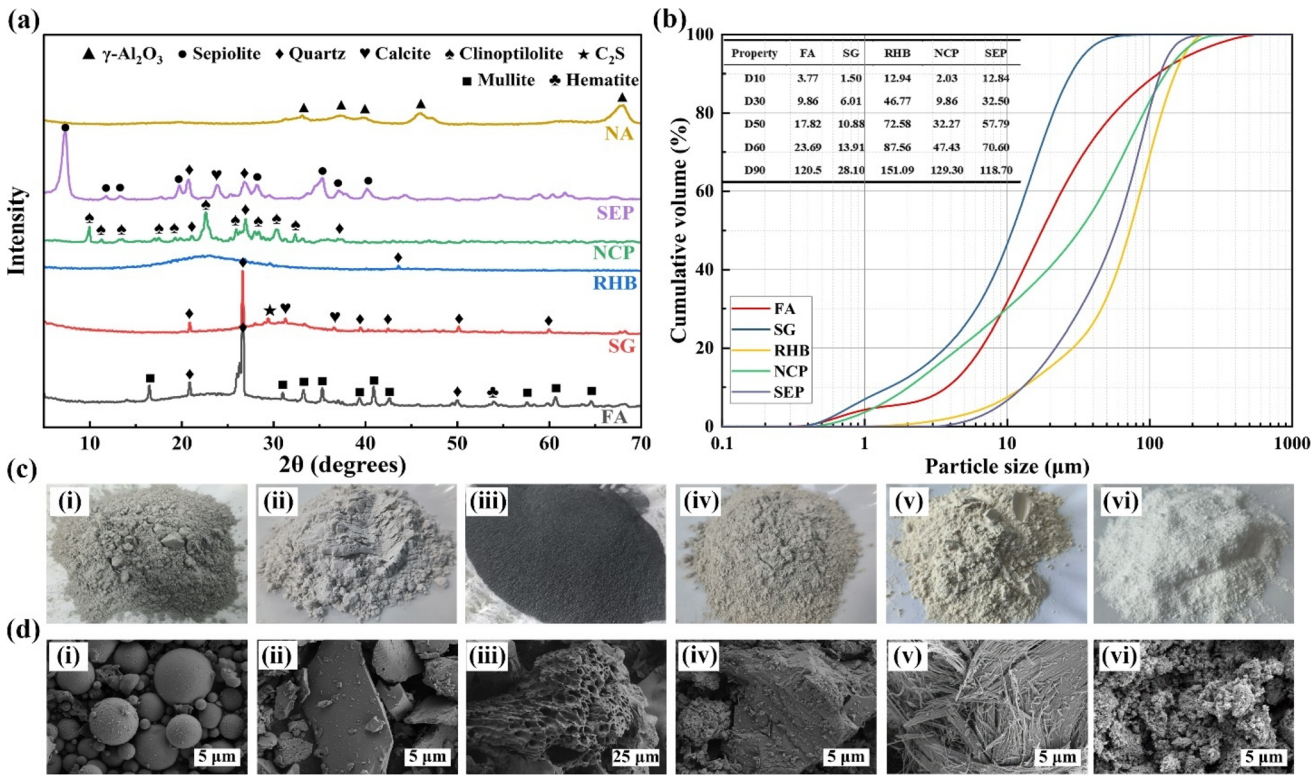


Fig. 1 Characterization of the raw materials and modifiers. (a) XRD; (b) particle size distribution; (c) appearance morphology; (d) SEM; (i) FA; (ii) SG; (iii) RHB; (iv) NCP; (v) SEP (vi) NA.

Table 1 Basic characteristics and chemical composition of raw materials and modifiers[a]

| | FA | SG | RHB | NCP | SEP | NA |
|---|---|---|---|---|---|---|
| **Basic properties** | | | | | | |
| Color | Dark grey | Light grey | Black | Light yellow | Yellowish white | White |
| Morphology | Spherical | Blocky | Porous | Laminar | Fibrous | Spherical |
| BET surface area ($m^2\ g^{-1}$) | 0.97 | 1.06 | 86.11 | 19.69 | 229.29 | 140.59 |
| Single point adsorption total pore volume of pores ($cm^3\ kg^{-1}$) | 2.19 | 3.73 | 57.91 | 45.42 | 438.13 | 837.47 |
| *t*-Plot micropore volume ($cm^3\ kg^{-1}$) | 0.21 | 0.07 | 35.42 | 4.53 | 42.68 | 6.74 |
| BJH desorption average pore diameter (4*V*/*A*) (nm) | 11.16 | 14.84 | 4.15 | 13.30 | 12.10 | 19.30 |
| Proportion of particle sizes below 10 μm (%) | 31.73 | 46.58 | 7.45 | 30.14 | 6.68 | 100.00 |
| **Chemical composition (wt%)** | | | | | | |
| CaO | 2.08 | 39.49 | 0.60 | 4.59 | 0.38 | — |
| $SiO_2$ | 53.43 | 26.92 | 41.12 | 64.61 | 58.01 | — |
| $Al_2O_3$ | 31.93 | 16.23 | 0.21 | 12.78 | 1.74 | 99.99 |
| $Fe_2O_3$ | 3.36 | 0.99 | 0.15 | 1.65 | 0.42 | — |
| $K_2O$ | 1.29 | 0.51 | 0.96 | 3.80 | 0.56 | — |
| $TiO_2$ | 1.18 | 1.14 | 0.01 | 0.20 | 0.08 | — |
| MgO | 0.53 | 9.93 | 0.33 | 1.01 | 24.15 | — |
| $P_2O_5$ | — | 2.12 | 0.36 | 0.02 | — | — |
| $SO_3$ | 0.53 | 2.12 | 0.07 | 0.04 | — | — |
| $P_2O_3$ | 0.18 | 0.05 | — | — | — | — |
| $Na_2O$ | — | — | 0.17 | 0.65 | 0.24 | — |
| Others (including other trace oxides and LOI) | 5.49 | 2.62 | 56.02 | 10.65 | 14.42 | 0.01 |

[a] LOI: loss on ignition.

number of pores of about 10 μm visible on the surface, exhibiting a loose and porous structure. As shown in Table 1, except for RHB, the micropore content (*t*-plot method) of the other modifiers is below 10%, confirming that their pore structure is primarily mesoporous. This also indicates that the mesopores in RHB are relatively scarce compared to its macropores and micropores.

**2.1.2. Alkali activator, $CO_2$ and high-salinity mine water.** The alkali activators used were NaOH (SH) and $Na_2SiO_3$ (SS), both purchased from Tianjin Hengxing Chemical Reagent Manufacturing Co., Ltd. The $CO_2$ gas was supplied by Xuzhou Luyou Gas Co., Ltd. The high-salinity mine water (HSW) was sourced from the 1309 working face at the Dananhu No. 1 Mine, Xinjiang Hami. The water quality analysis results are shown in Table 2. According to the analysis, the cation composition of the water sample is predominantly $Na^+$, with significant concentrations of $Ca^{2+}$ and $Mg^{2+}$. The dominant anions are $Cl^-$ and $SO_4^{2-}$, classifying the water as $Cl{\cdot}SO_4$–Na type mine water. No heavy metal components listed were detected in the raw water sample. The initial pH value was measured at 7.33, indicating weak alkalinity. The total dissolved solids (TDS) concentration was determined to be 29 017 mg $L^{-1}$, with an electrical conductivity of 46 100 μS $cm^{-1}$, characteristic of typical high-salinity mine water. Other relevant ion concentrations and parameters are detailed in the table.

## 2.2. Preparation

The preparation of CCB was optimized following the GB/T 17671-2021,[29] with material ratios detailed in Table 3. Initially,

Table 2 Quality analysis results for the high-salinity mine water

| Test item (common ions) | | Test result (mg $L^{-1}$) | Test item (heavy metals) | Test result (mg $L^{-1}$) | Other test items | Test result |
|---|---|---|---|---|---|---|
| Cations | $K^+$ | 32.10 | Cr | — | pH | 7.33 |
| | $Na^+$ | 9061.00 | Ni | — | TDS (mg $L^{-1}$) | 29 017.00 |
| | $Ca^{2+}$ | 705.00 | Cu | — | Alkalinity (mg $L^{-1}$) | 258.00 |
| | $Mg^{2+}$ | 404.00 | Zn | — | Total hardness (mg $L^{-1}$) | 3427.00 |
| | $NH_4^+$ | 6.20 | As | — | Conductivity (μS $cm^{-1}$) | 46 100.00 |
| Anions | $HCO_3^-$ | 315.20 | Cd | — | Suspended solids (mg $L^{-1}$) | — |
| | $Cl^-$ | 12 210.00 | Pb | — | Turbidity (NTU) | — |
| | $SO_4^{2-}$ | 6437.00 | Be | — | Color | None |
| | $CO_3^{2-}$ | 0.00 | Ag | — | Odor & taste | None |
| | $NO_2^-$ | 0.04 | Mn | — | Visible substances | Precipitate |

the raw materials and modifiers were thoroughly dry blended at low speed for 30 seconds to ensure uniform solid-phase distribution. Separately, SS and SH were dissolved in the deionized water and stirred at 500 rpm for 10 min to prepare the alkaline activator. The solid mixture was then combined with the liquid phase and transferred to a reactor, with continuous $CO_2$ injection at a rate of 1 L $min^{-1}$. After reaching the designated time, the fresh slurry was poured into a $\Phi$ 50 mm × 100 mm cylindrical mold and allowed to cure at room temperature for 48 h before being demolded. The sample was then transferred to a standard curing chamber (temperature 20 ± 2 °C; humidity 95 ± 2%) for curing.

### 2.3. Methods

**2.3.1. Toxicity characteristic leaching protocol (TCLP)—EPA-1311.** The leaching characteristics of heavy metals (Cr, Ni, Cu, Zn, As, Cd, Pb, Be, Ag, and Mn) in the CCB were evaluated in triplicate ($n = 3$) according to the EPA-1311 standard.[30] The cured CCB samples were crushed, and fragments from the central region were ground and passed through a 0.99 mm sieve. The extraction fluid used in the TCLP test was obtained by adding an amount of 0.1 mol $L^{-1}$ acetic acid solution to deionized water until the pH value was 2.88 ± 0.05. The samples were mixed with $L/S$ of 20.0 mL $g^{-1}$ for 18 h using a flip-type oscillator at 30 ± 2 rpm, with gas being vented every hour.

Following filtration, the leachate samples were immediately subjected to *aqua regia* digestion ($HNO_3 : HCl = 1 : 3$) to prevent metal precipitation and match the calibration standards. Specifically, the samples were heated in a water bath with 5 mL of *aqua regia* until clear, cooled to 60 °C, and diluted to 25 mL with deionized water. The concentrations of target heavy metals were determined using an ICP-MS (Agilent 7800, USA) operating in kinetic energy discrimination (KED) mode to effectively eliminate polyatomic interferences. Quantification was performed using an external standard method with internal standard correction. Multi-element standard solutions, ranging from 0 to 500 μg $L^{-1}$, were used to establish calibration curves, all of which exhibited excellent linearity ($R^2 > 0.999$). To compensate for matrix effects and instrumental drift, $^{103}Rh$ and $^{185}Re$ were employed as internal standards. Detailed methodological parameters, including the standard series, limits of detection (LOD), limits of quantification (LOQ), and raw calibration data, are provided in SI Table S1.

**2.3.2. Long-term static leaching experiment.** The cured samples ($n = 3$ per group) were immersed in a corrosion-resistant tank containing sufficient high-salinity mine water, maintained at least 20 mm above the sample surface to ensure full coverage. The tests were conducted at room temperature with sealing film and sealed lids to reduce evaporation. Soaking durations were set at 1, 3, 7, 14, 30, and 60 d. Throughout the period, the pH of the solution were measured using a pH meter (Shanghai Yueping PHS-25).

**2.3.3. Uniaxial compressive strength (UCS) test.** The samples after soaking were placed in an ethanol solution for 4 h to terminate the hydration, and dried at 80 °C for 24 h until a constant weight. Then the uniaxial compressive strength (UCS) was tested according to the standard GB/T 23561.7-2009 (ref. 31) using a WANCE HUT605A electro-hydraulic servo-controlled rock testing machine at a loading rate of 0.5 MPa $s^{-1}$.

**2.3.4. Porosity test.** Another set of samples was prepared for porosity test using the water saturated method. The samples were first immersed in absolute ethanol for 4 h to terminate the hydration, then dried at 80 °C until constant weight. After being cooled to ambient temperature, the dry sample was weighed and submerged within the deionized water in the sealed bottle. The bottle was then vacuumed at −0.1 MPa for 2 h to ensure that the sample was fully saturated. After that, the saturated samples were surface-dried and immediately weighed. Then using the drainage method, each saturated sample was immersed in the deionized water, and the mass of displaced water—corresponding to the total sample volume—was measured. The porosity is calculated as follows:

$$V_w = \frac{M_w}{\rho_w} \quad (1)$$

$$\varphi = \frac{(M_s - M_d)/\rho_w}{V_t} \times 100\% \quad (2)$$

where $V_w$ is the volume of water inhaled, $M_w$ is the mass of water inhaled, $\rho_w$ is the density of the water, $\varphi$ is the porosity of the sample, $M_s$ is the saturated mass of the sample, $M_d$ is dried mass of the sample, and $V_t$ is the total volume of the sample.

Table 3 Composition ratio of the CCB slurry

| | Solid mass percentage | | | Liquid mass percentage | | | | | | Modifier | | | |
|---|---|---|---|---|---|---|---|---|---|---|---|---|---|
| No. | FA/wt% | SG/wt% | Solid/wt% | DW/wt% | HSW/wt% | SS/wt% | SH/wt% | Liquid/wt% | $CO_2$/min | RHB/wt% | NCP/wt% | SEP/wt% | NA/wt% |
| CCB | 80 | 20 | 70 | 46.25 | 46.25 | 5 | 2.5 | 30 | 20 | — | — | — | — |
| CCB-R | 80 | 20 | 67 | 46.25 | 46.25 | 5 | 2.5 | 30 | 20 | 3.00 | — | — | — |
| CCB-N | 80 | 20 | 67 | 46.25 | 46.25 | 5 | 2.5 | 30 | 20 | — | 3.00 | — | — |
| CCB-S | 80 | 20 | 67 | 46.25 | 46.25 | 5 | 2.5 | 30 | 20 | — | — | 3.00 | — |
| CCB-RN | 80 | 20 | 67 | 46.25 | 46.25 | 5 | 2.5 | 30 | 20 | 1.50 | 1.50 | — | — |
| CCB-RS | 80 | 20 | 67 | 46.25 | 46.25 | 5 | 2.5 | 30 | 20 | 1.50 | — | 1.50 | — |
| CCB-Rn | 80 | 20 | 67 | 46.25 | 46.25 | 5 | 2.5 | 30 | 20 | 2.90 | — | — | 0.10 |
| CCB-RNn | 80 | 20 | 67 | 46.25 | 46.25 | 5 | 2.5 | 30 | 20 | 1.45 | 1.45 | — | 0.10 |
| CCB-RSn | 80 | 20 | 67 | 46.25 | 46.25 | 5 | 2.5 | 30 | 20 | 1.45 | — | 1.45 | 0.10 |

**2.3.5. Microstructure analysis.** The central portion of samples after UCS test was collected and sieved through a 200-mesh sieve. X-ray diffraction (XRD) analysis was performed using a Puxi General XD-6 diffractometer with Cu K$\alpha$ radiation ($\lambda = 1.54184$ Å). Data were collected over a $2\theta$ range of 5° to 70° at a scanning rate of 2° $min^{-1}$. Phase identification was conducted using MDI Jade software.

The microstructure and elemental composition were examined by field emission scanning electron microscopy (SEM, ZEISS Sigma 300) equipped with energy dispersive spectroscopy (EDS, OXFORD X-max 50). Samples were dried and mounted on conductive adhesive tape. Observations were made under high vacuum at 2 kV accelerating voltage.

**2.3.6. Functional group analysis.** FTIR spectroscopy was performed using an infrared spectrometer (Thermo Fisher Nicolet iS20 spectrometer). The wave number ranged from 4000–400 $cm^{-1}$ with a spectral resolution of 4 $cm^{-1}$, and 32 scans were set for all FTIR scans. The spectra were corrected using baseline and normalized for comparisons.

# 3. Results

## 3.1. Immobilization behavior of heavy metals in modified samples

**3.1.1. TCLP leaching characteristics of raw materials.** Fig. 2 presents the results of the TCLP tests conducted on FA and SG. The regulatory thresholds from Class III and Class IV groundwater quality standards (III-GQS and IV-GQS), based on the GB/T 14848-2017,[32] are also shown. Among the 10 heavy metals tested, 6 and 2 toxic elements in FA and SG, respectively, exceeded the III-GQS limits. FA generally exhibited more heavy metals species with leaching concentrations above the threshold. In particular, the concentrations of Cr, Ni, As, and Mn reached 1002.57 ± 28.47, 151.07 ± 5.89, 181.16 ± 6.15, and 1910.14 ± 34.38 μg $L^{-1}$, respectively, all exceeding the limits of the IV-GQS. In contrast, Pb (30.17 ± 1.47 μg $L^{-1}$) and Be (22.43 ± 1.41 μg $L^{-1}$) only exceeded the III-GQS limits but still complied with the IV-GQS, while the leaching concentrations of Cu, Zn, Cd, and Ag directly satisfied the III-GQS. Compared with FA, SG showed slightly lower toxicity. Most elements, such as Cr, Ni, Cu, Zn, As, Pb, and Be, were significantly below the III-GQS limits, and the concentration of Cd was below the limit of detection (LOD, not detected). However, the concentrations of Ag and Mn were far higher than the IV-GQS limits, reaching 2239.39 ± 64.94 μg $L^{-1}$ and 7613.53 ± 137.04 μg $L^{-1}$, respectively.

Comparative analysis revealed that FA had significantly higher leaching concentrations of Cr, Ni, Cu, Zn, As, Cd, Pb, and Be than SG ($p < 0.05$). Excluding Cd, the average leaching levels of these elements in FA were approximately 57 times higher than in SG, with more elements exceeding regulatory limits. Although only Ag and Mn in SG exhibited higher leaching than in FA—Mn being roughly four times higher—the absolute leaching concentrations of these two elements in SG were substantially greater by 2238.20 μg $L^{-1}$ and 5703.39 μg $L^{-1}$, respectively. These differences likely arise from the distinct origins and physicochemical properties of the materials. Overall, considering both the number of elements and concentrations exceeding III-GQS and IV-GQS thresholds, FA poses a higher leaching risk than SG.

**3.1.2. TCLP leaching characteristics of modified samples.** Fig. 3 presents the leaching concentrations of heavy metals in each sample (all detailed TCLP data and their comparison with the GQS are presented in SI Table S2). It can be seen that, after being mixed with high-salinity water and prepared into CCB, the heavy metals leaching from the raw materials (FA and SG)

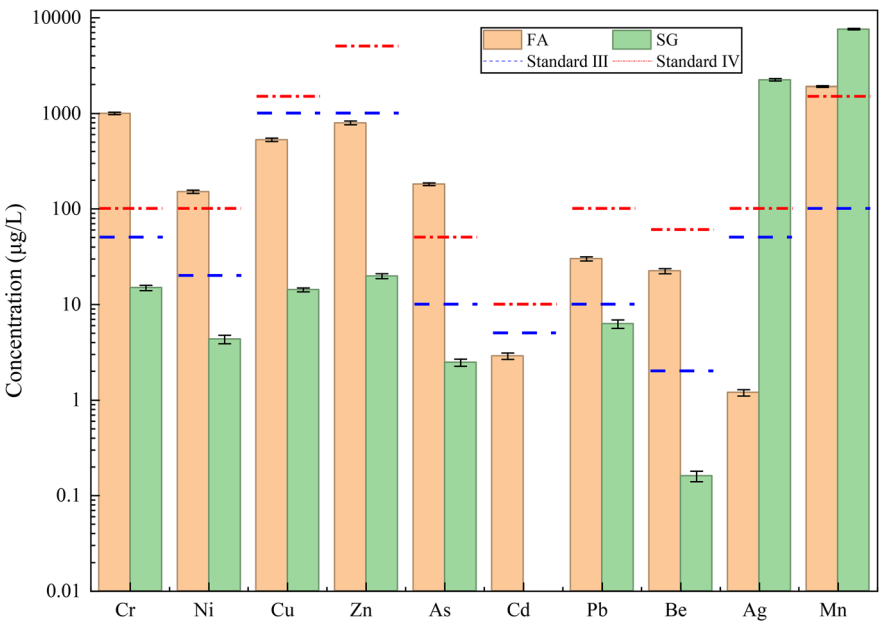


Fig. 2 TCLP leaching results of FA and SG.

was significantly suppressed. For the unmodified CCB, the leaching concentrations of Cr, Ni, Cu, Zn, As, Cd, Pb, Be, Ag, and Mn were reduced by 82.05%, 23.42%, 86.05%, 87.37%, 80.88%, 30.06%, 27.29%, 71.56%, 94.49%, and 10.63%, respectively, compared with the weighted sum of FA and SG (according to their mixing ratio). This highlights the critical role of hydration and carbonation reactions in the immobilization of heavy metals.[7] Nevertheless, leaching concentrations of Cr and Mn still exceeded the IV-GQS regulatory limits, and Ni was marginally below this threshold. For As, Pb, and Be, although below IV-GQS, levels exceeded the stricter III-GQS limits. This suggests that mixing and $CO_2$ carbonation alone are insufficient to achieve complete stabilization of all heavy metals, and further modification is required to enhance the environmental safety of CCB.

In the single-modifier systems, the leaching concentrations of most heavy metals are lower than those of the unmodified group. However, its control of certain elements remains a worse effect. For example, RHB failed to reduce the Mn concentration below the IV-GQS limit, and the leaching concentration of As even rose to $34.42 \pm 2.54$ μg $L^{-1}$.[33] Only the introduction of NCP exhibited a notably weaker immobilization capacity for Ag. By contrast, SEP used alone showed the most pronounced improvement. The leaching concentrations of Ni, Cu, Zn, As, Cd (below the LOD), Pb, Be (below the LOD), Ag, and Mn decreased by approximately 74.29%, 84.21%, 89.80%, 35.09%, 97.95%, 81.67%, 100.00%, 88.17%, and 76.68%, respectively ($p < 0.05$). Nevertheless, SEP alone still showed a limitation in immobilizing Cr, with its leaching concentration of $101.22 \pm 4.25$ μg $L^{-1}$ slightly exceeding the IV-GQS limit for Cr (100 μg $L^{-1}$). Overall, SEP alone reduced the average leaching of heavy metals by approximately 75.78% ($p < 0.05$). On this basis, although the combined use of modifiers to some extent reduces the control efficiency for certain heavy metals compared with the best-performing single modifier, it still maintains their leaching concentrations below the IV-GQS limits, while compensating for the inadequate control of specific heavy metals by individual modifiers. For instance, in the CCB-RN system, the synergistic use of RHB and NCP overcame the insufficient control of Mn, As, and Ag observed when each is used alone, and further enhanced the immobilization of Be, reducing its leaching concentration to below the III-GQS limit. In the CCB-RS group, although the fixation of Ni, Cu, and Zn was slightly inferior to that achieved with SEP alone, a synergistic enhancement was observed for Cr and Ag. The leaching concentration of Cr decreased by 48.52% and 83.18% relative to CCB-R and CCB-S, respectively ($p < 0.05$), and was reduced from exceeding the IV-GQS limit to within the III-GQS range.

Previous studies have shown that the adsorption capacity of materials is closely related to the adsorption sites provided by their rich pore structure.[34] Considering that the addition of NA fills the pores within the material, it is likely to weaken the adsorption capacity of the CCB for heavy metals. However, when comparing CCB-R and CCB-Rn, the introduction of NA further reduced the leaching concentrations of Cr, Cu, Zn, As, Cd, Pb, Be, and Mn in CCB-RN by 52.36%, 59.17%, 44.72%, 21.98%, 7.96%, 28.18%, 90.13%, and 28.52% respectively on average ($p < 0.05$). However, in the CCB-RNn and CCB-RSn systems, the leaching concentrations of Cr, Ni, Ag, and Mn increase compared to CCB-RN and CCB-RS, with the increase being more significant in CCB-RNn. This suggests that when NA is combined with RHB, it not only does not weaken the immobilization effect but actually enhances the suppression of certain heavy metals. However, when NA is used in combination with clay materials (such as NCP and SEP), the immobilization effect is weakened. This may be because NA has less impact on the

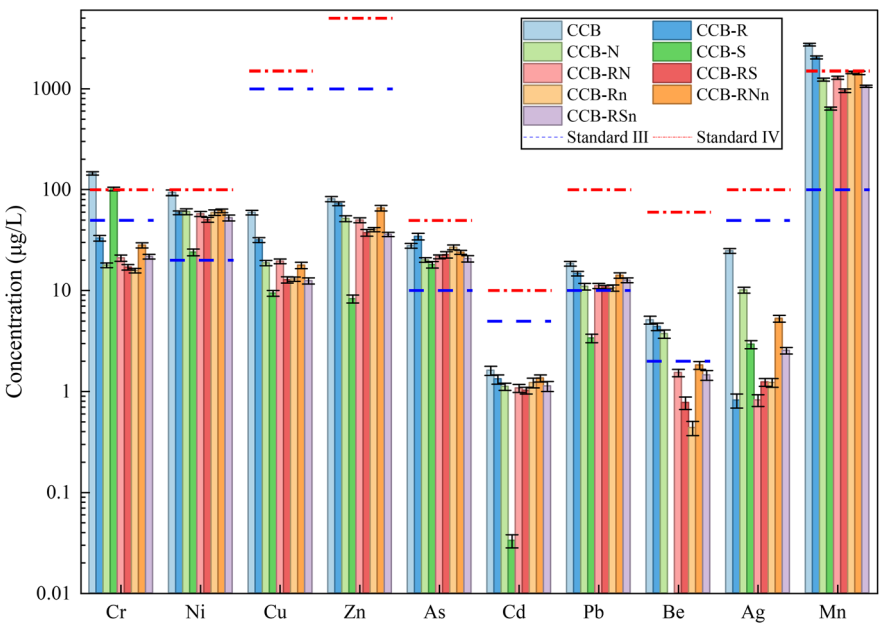


Fig. 3 TCLP leaching results of modified samples.

overall pore structure when combined with RHB, but when combined with clay materials, the pores between the different materials are more likely to fill each other, leading to a reduction in the total porosity. The damage to the pore structure of NCP is particularly noticeable, which weakens the overall immobilization capacity of the system for heavy metals.

### 3.2. Evolution of macroscopic properties and solution pH of modified backfill

Fig. 4 shows the changes in the UCS, porosity, and solution pH over time for different modified backfill during high-salinity water soaking. Detailed experimental data are provided in SI Tables S3–S5, respectively.

According to Fig. 4a, all samples initially experienced a strength decrease due to slight surface dissolution.[35] As continued soaking, most samples showed gradual strength recovery, suggesting that cations like $Ca^{2+}$ and $Mg^{2+}$ provided by high-salinity water promoted further hydration. Notably, CCB and CCB-N underwent significant strength loss after 60 d (−11.62% and −7.84%, respectively, $p < 0.05$), likely caused by expansive products formed from high ion concentrations, leading to micro-cracking.[36] In contrast, samples modified with RHB, SEP, or NA maintained strength growth, reflecting superior long-term durability. The impact of RHB and NCP on strength is more complex. At 3 wt% RHB content, the backfill showed an average strength decrease of 5.91% across all soaking periods compared with CCB ($p < 0.05$), whereas reducing the dosage to 1.5 wt% led to a strength increase. This can be attributed to the aggregation effect caused by excessive biochar, which creates weak zones within the CCB.[37] NCP similarly reduced strength, further influenced by its low pozzolanic reactivity due to higher stable crystalline $SiO_2$ content.[38] The introduction of SEP significantly increased the backfill UCS by an average of 51.3% across all soaking periods compared with CCB ($p < 0.05$). Furthermore, its UCS continued to increase even after 60 d of soaking, reaching 10.07 ± 0.16 MPa. This remarkable long-term durability is owing to its high surface area that supports continuous hydration, and its fibrous straw-bundle structure which forms an interwoven network to disperse stress.[39] Introducing NA further improved the strength of the three sample groups (*e.g.*, CCB-RSn averaged 15.98% higher than CCB-RS across all soaking periods, $p < 0.05$). This enhancement is likely due to the nanomaterial's filling effect and its direct participation in hydration to promote gel formation.[40]

Porosity tests (Fig. 4b) show that all samples experienced a temporary increase in porosity during the initial immersion phase due to the rapid dissolution of soluble salts. Subsequently, as hydration gels continuously formed, the structure became denser, leading to a gradual decrease in porosity.[41]

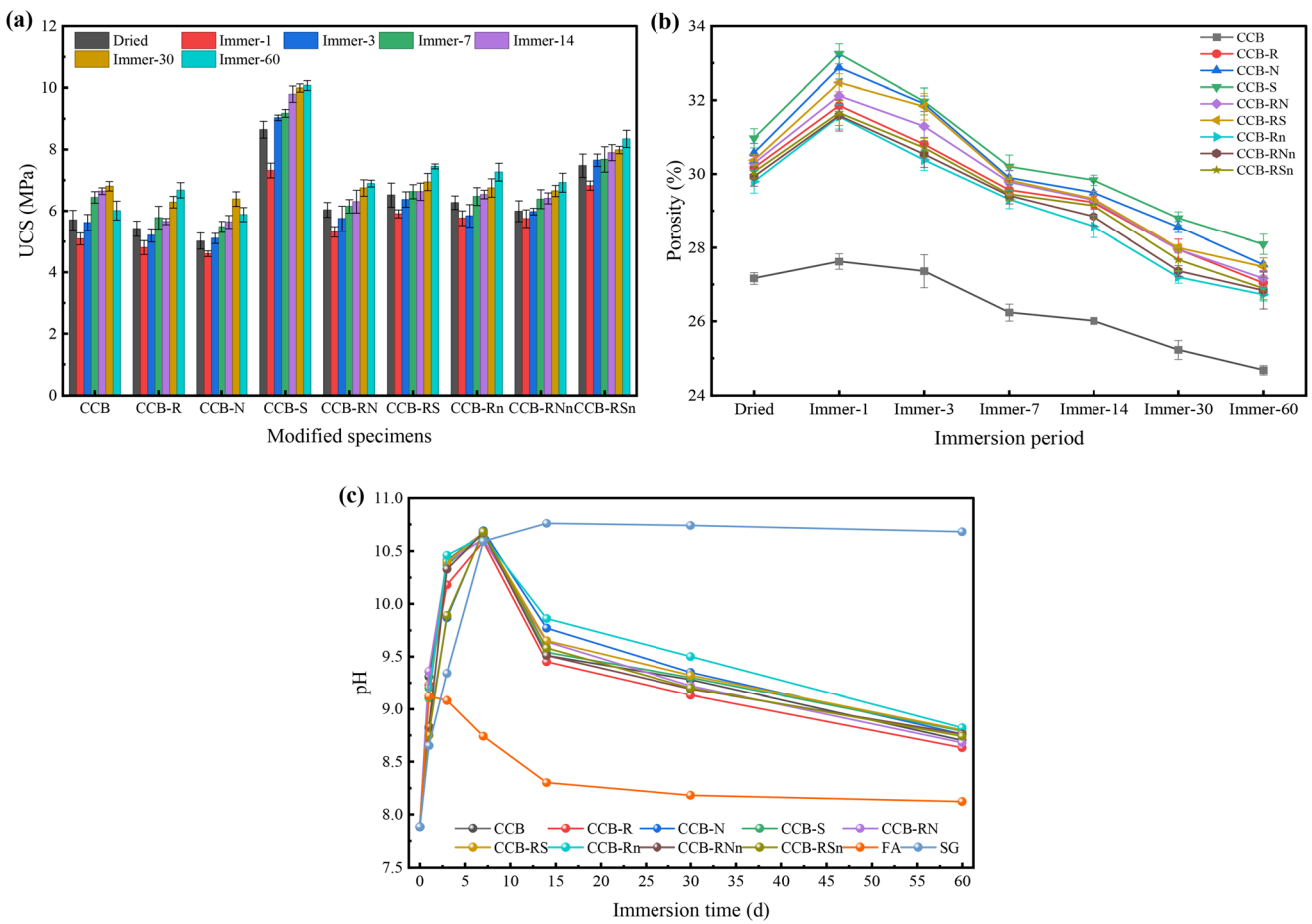


Fig. 4 Evolution of macroscopic properties and solution pH of modified backfill: (a) UCS; (b) porosity; (c) solution pH.

Compared to the CCB, all modified samples showed a significant increase in porosity. SEP had the most significant impact on porosity of CCB. As shown in Table 1, the total pore volume of SEP is second only to that of NA, and its particles are relatively coarse (with only 6.68% of particles below 10 μm), making it difficult to embed within the larger pores of RHB, leading to a relatively independent distribution. Additionally, its average pore diameter is only 12.10 nm, much smaller than the average particle size of the raw materials and NA (average particle size: 40 nm), which would require larger filling space. This allows the high pore volume of SEP to be effectively retained, significantly increasing the overall porosity. When NCP was used alone for modification, a similar mechanism was observed. However, its finer particles (30.14% below 10 μm) could more easily fill the larger pores of RHB, reducing its overall contribution to the porosity. After the NA introduction, the porosity of the samples (CCB-Rn, CCB-RNn, CCB-RSn) decreased by an average of 1.50%, 1.63%, and 1.78% across all soaking periods compared with non-NA groups ($p < 0.05$) due to the nanoparticles filling pores and promoting densification.[42]

The changes in solution pH (Fig. 4c) further reveal the reaction process within the system. All samples showed a rapid pH increase during the initial soaking period (0–7 d), rising from 7.33 to about 11.00, primarily due to the rapid dissolution of cementitious materials releasing a large amount of $OH^-$.[35] Subsequently, the pH gradually declined due to the ongoing consumption of $OH^-$ by hydration. To verify that this pH decline was not caused by atmospheric $CO_2$ interference, supplementary acid–base-titration experiments were conducted, which confirmed that internal hydration dominated the $OH^-$ consumption (titration curves and detailed analyses are provided in SI Fig. S1). Additionally, when pH fell within the range of 8–10, part of carbonates transformed into more soluble bicarbonates that dissociated to release $H^+$, further lowering the pH.[43] For FA and SG, the initial pH increase was driven by the rapid dissolution of $Ca^{2+}$ and $Mg^{2+}$, forming hydroxides and subsequently releasing $OH^-$. As the

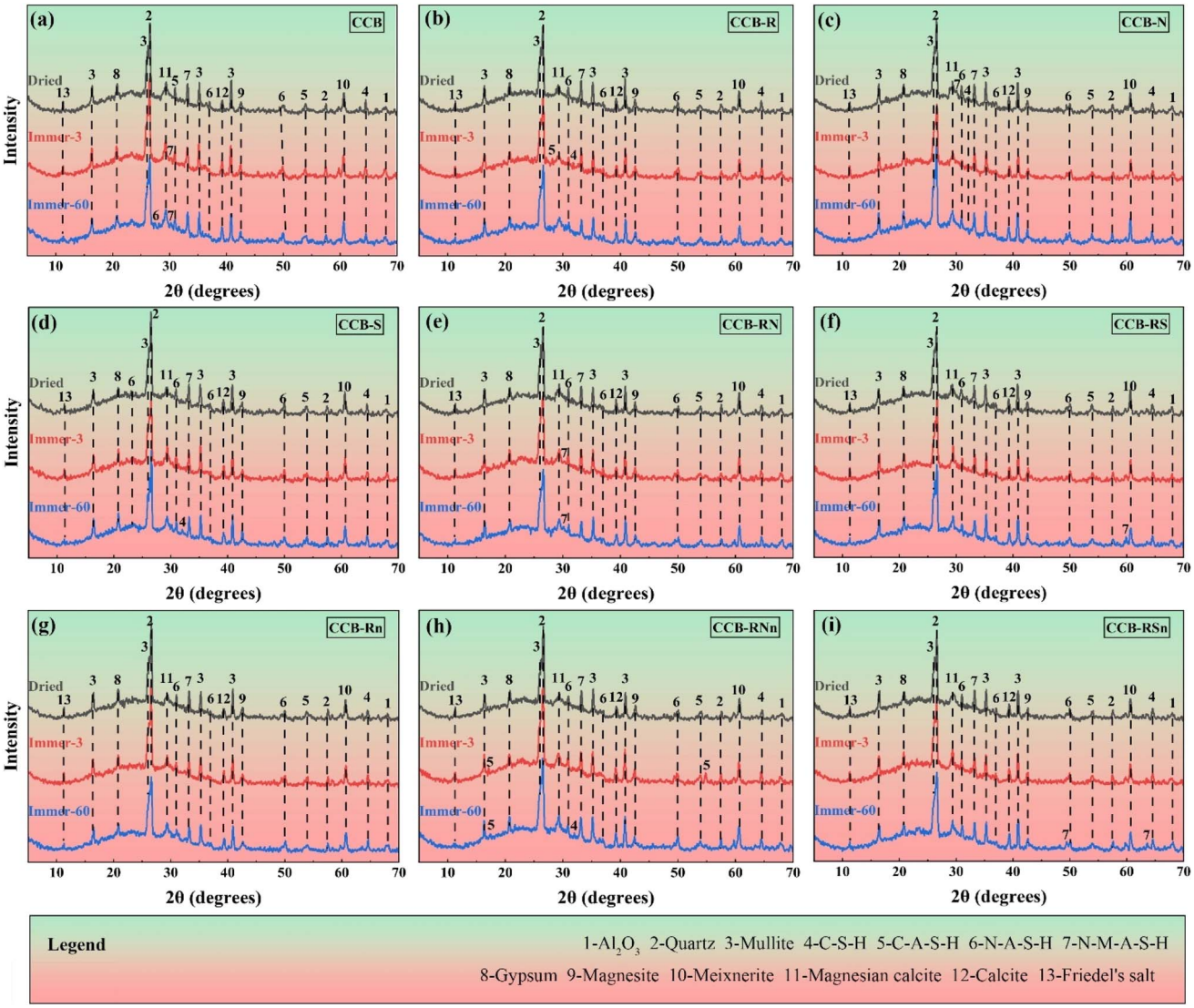


Fig. 5 XRD patterns of each group of samples. (a) CCB; (b) CCB-R; (c) CCB-N; (d) CCB-S; (e) CCB-RN; (f) CCB-RS; (g) CCB-Rn; (h) CCB-RNn; (i) CCB-RSn.

reaction progressed, the ionization of $OH^-$ reached a limit, and as the pH increased, $SiO_2$ and $Al_2O_3$ within the system began to react and consume $OH^-$, forming $SiO(OH)_3^-$ and $Al(OH)_4^-$ (key precursors for pozzolanic reactions), which again lowered the pH. The reaction equations are given in eqn (3)–(6). XRF analysis reveals that FA contains less CaO and MgO but more $SiO_2$ and $Al_2O_3$ than SG, therefore its pH was lower and declined more rapidly later. In contrast, the different modifiers had little impact on the overall pH evolution of the system.

$$CaO + H_2O \rightarrow Ca(OH)_2 \rightarrow Ca^{2+} + 2OH^- \quad (3)$$

$$MgO + H_2O \rightarrow Mg(OH)_2 \rightarrow Mg^{2+} + 2OH^- \quad (4)$$

$$SiO_2 + H_2O + OH^- \rightarrow SiO(OH)_3^- \quad (5)$$

$$Al_2O_3 + 3H_2O + 2OH^- \rightarrow 2Al(OH)_4^- \quad (6)$$

### 3.3. Heavy metal immobilization mechanisms in modified backfill

**3.3.1. Evolution of hydration products and crystalline phases.** Fig. 5 compares the XRD spectra of samples in dry state and after 3 and 60 d of soaking. The main hydration products include C-S-H, C-A-S-H, N-A-S-H, and N-M-A-S-H gels. Carbonation primarily yields magnesian calcite ((Ca, Mg)$CO_3$), along with magnesite ($MgCO_3$) and calcite ($CaCO_3$). Additionally, under the influence of high-salinity water, gypsum ($CaSO_4 \cdot 2H_2O$) and Friedel's salt ($Ca_4Al_2(OH)_{12} \cdot Cl_2 \cdot 4H_2O$) also formed as secondary phases. Residual minerals detected include $Al_2O_3$, quartz, mullite, and meixnerite ($Mg_6Al_2(OH)_{18} \cdot 4H_2O$).

Hydration gels, mainly C-S-H, are the primary products from the CCB hydration. After carbonation, the decreased Ca/Si ratio promotes Al incorporation into the gel network, yielding the C-A-S-H gel phase ($2\theta = 54.5°$).[41] In high-salinity water, ions exchange and adsorption with cations (*e.g.*, $Na^+$, $Mg^{2+}$) further transform the gels into N-A-S-H and N-M-A-S-H,[35] with characteristic peaks at $2\theta = 31.1°$, 33.1°, and 50.1°. After modification, the peak intensities of the two new gel phases increased slightly, especially in the SEP group, due to its high Mg content. A broad hump peak at $2\theta = 20–35°$ indicates the presence of amorphous silica gel, which exhibits higher reactivity $SiO_2$. Carbonate phases—magnesian calcite, magnesite, and calcite—appear at $2\theta = 29.5°$, 43.0°, and 39.3°, respectively. Gypsum ($2\theta = 20.7°$) and Friedel's salt ($2\theta = 11.3°$), a layered double hydroxide (LDH), also arise form under high $Cl^-$ and $SO_4^{2-}$

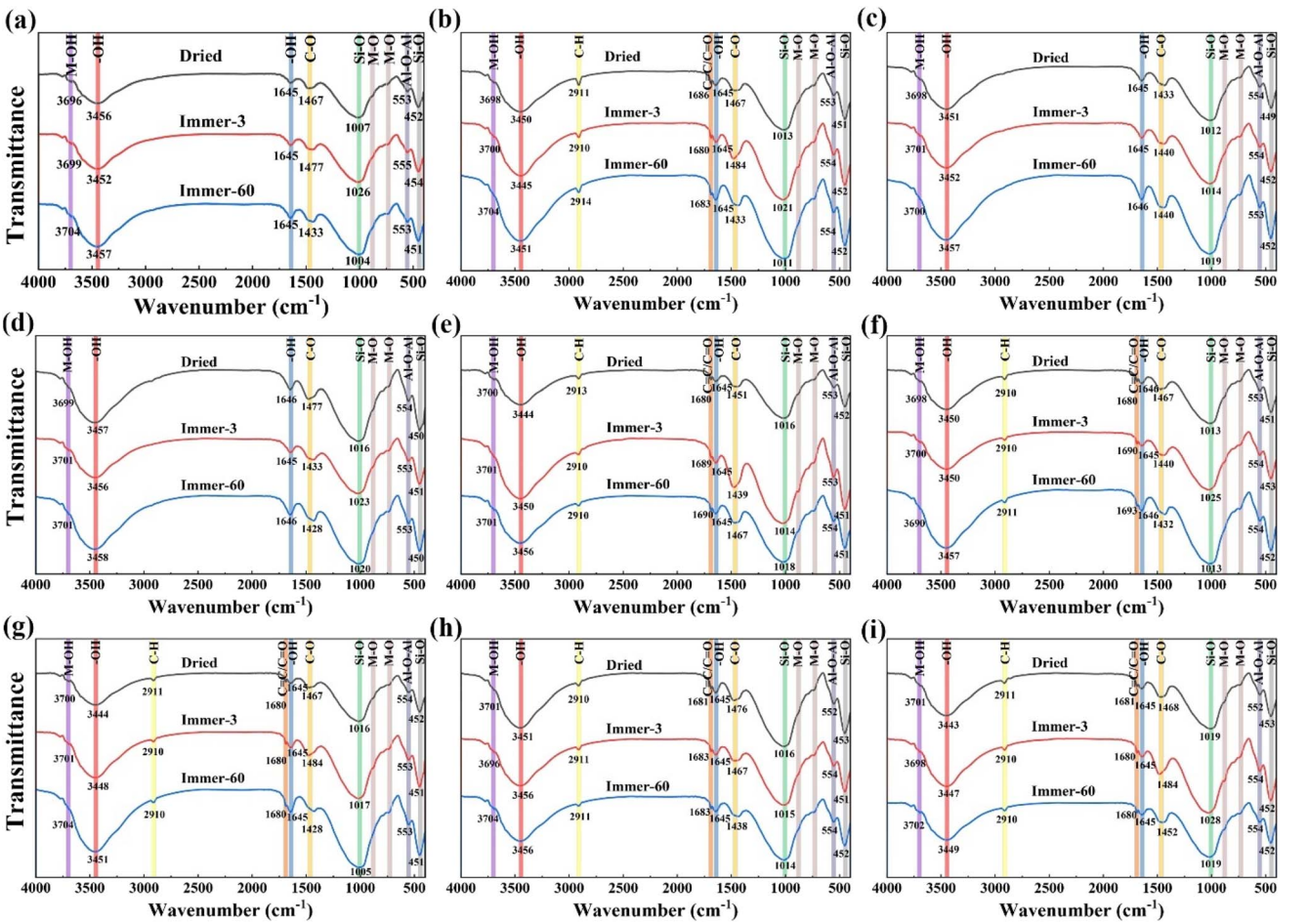


Fig. 6 FTIR spectral of each group of samples. (a) CCB; (b) CCB-R; (c) CCB-N; (d) CCB-S; (e) CCB-RN; (f) CCB-RS; (g) CCB-Rn; (h) CCB-RNn; (i) CCB-RSn.

concentrations. Additionally, meixnerite, identified at $2\theta$ = 60.8°, is another Mg–Al hydrotalcite with a bilayer structure.[44] No significant phase differences were observed with different modifiers, likely owing to their high stability and low addition.

**3.3.2. Evolution of functional groups and chemical bonds.** Fig. 6 presents the FTIR spectra of each sample group within the 400–4000 $cm^{-1}$ wavenumber range, with key absorption peaks clearly identified. All samples exhibit a strong absorption peak near 3450 $cm^{-1}$ and a weaker peak around 3700 $cm^{-1}$, corresponding respectively to the stretching vibrations of crystalline water hydroxyl groups (–OH) and structural hydroxyl groups (M–OH).[45] The structural hydroxyl groups primarily originate from the crystal structure of layered double hydroxides (LDHs), where M represents Mg, Al, or Ca. Notably, the modified samples display enhanced intensities for these peaks, indicating increased lattice water and structural hydroxyl content. Bending vibrations of interlayer free water (H–O–H) are observed at approximately 1645 $cm^{-1}$.[46] A prominent peak near 1000 $cm^{-1}$ is attributed to the asymmetric stretching vibration of Si–O within silicon–oxygen tetrahedra.[47] Particularly in the NA-modified groups, the absorption intensities at both 3450 $cm^{-1}$ and 1000 $cm^{-1}$ are relatively strengthened compared to the non-NA groups. This spectral evidence indicates a higher abundance of structural hydroxyls and silanol groups induced by NA, which can serve as vital active sites for subsequent heavy metal immobilization. In the lower wavenumber region, Si–O bending vibrations and Al–O absorption peaks appear at approximately 450 $cm^{-1}$ and 550 $cm^{-1}$, respectively. A distinct peak at 1450 $cm^{-1}$ corresponds to the asymmetric stretching vibration of C–O, associated with carbonates formed during carbonation.[48] However, no absorption peak corresponding to S–O is observed in the spectra. This may because the bending vibration peak of $SO_4^{2-}$ is located at approximately 1110 $cm^{-1}$, which is very close to the strong asymmetric stretching peak of Si–O,[49] and therefore be obscured by it. Moreover, due to the lack of spectral absorption characteristics of $Cl^-$, its presence cannot be directly identified.[50] The sample modified with RHB exhibits additional stretching vibration peaks at 1680 $cm^{-1}$ and 2910 $cm^{-1}$, corresponding to C=C/C=O and C–H bonds,[51] respectively, suggesting the introduction of oxygen-containing functional groups such as –COOH. These functional groups are beneficial for mitigating Heavy metals leaching.

Two absorption peaks within 400–800 $cm^{-1}$ are assigned to M–O vibrations, where M may include Mg, Al, Ca, or heavy metals (HMs). Specifically, a comparison between the Dried group and the Immer-3 or Immer-60 groups reveals that these M–O peaks undergo corresponding shifts in position and intensity throughout the immersion period. This phenomenon indicates that Mg(Al, Ca)–O bonds are being transformed into HMs–O bonds through chemical adsorption and surface complexation,[49] thereby providing direct evidence for the "re-adsorption" of heavy metals. This process is further facilitated by the abundant oxygen-containing functional groups (*e.g.*, –OH and –COOH) introduced by the modifiers, particularly biochar, which serve as active sites for trapping heavy metal ions. These slight shifts in peak positions and intensities after modification and immersion in high-salinity solutions reflect changes in stretching or bending vibrations, indicative of the active immobilization of heavy metals within the CCB matrix.

**3.3.3. Evolution of microscopic morphology.** Fig. 7 presents SEM-EDS images of samples under dry conditions. Under alkaline activation and high-salinity water rich in various cations, continuous hydration in CCB forms various gels. Microscopically, these gels show a honeycomb network structure with little visual variation, distinguishable mainly by EDS elemental analysis. Studies indicate that C-S-H and N-A-S-H gels are slightly less dense than C-A-S-H and N-M-A-S-H, which may account for the differences in their mechanical strength.[52] Additionally, dissolved $CO_2$ generates $CO_3^{2-}$ that reacts with activated $Mg^{2+}$ and $Ca^{2+}$, precipitating as crystalline carbonates. Calcite and magnesite display plate-like crystals, while magnesian calcite exhibits a similar morphology with surface clusters of fine crystals. In the presence of high concentrations of $SO_4^{2-}$ and $Cl^-$, laminar Friedel's salt crystals and oblique columnar gypsum crystals precipitate near the gel phase. The associated reactions are summarized in Table 4.

Fig. 8 illustrates the microstructural evolution of five sample groups (unmodified, –RHB, –NCP, –SEP–, and –NA) to clarify modifier effects. The overall trend shows progressive pore closure with soaking, consistent with the previous porosity evolution. During immersion, C-S-H gels interact with cations to form more complete hydration phases. Simultaneously, carbonates formed *via* carbonation, along with gypsum and Friedel's salt generated under anionic erosion, tend to aggregate through phase transformation-driven processes. These compounds nucleate and precipitate in crystalline forms, further developing within the porous structure.[53] Interestingly, although gypsum expansion is often associated with reduced durability and cracking in cement-based materials,[54] the UCS results indicate that the strength of the most samples increased with soaking time. This is attributed to the porous property of the modifiers, where abundant pore space accommodates expansion stresses. Nevertheless, microcracks observed in CCB and CCB-N at 60 d (Fig. 8(a-3) and (c-3)) correspond to their strength drop, indicating that the mesoporous structure of NCP provides insufficient space to accommodate expansion. In contrast, SEP-modified samples maintained strength improvement due to their robust fibrous structure (Fig. 8d).

It should be noted that although the reduction in porosity improves the strength of the sample, it also reduces the contact opportunities between the porous material and heavy metals in the solution, which may potentially lower its adsorption effect on heavy metals. At this point, the superiority of substances with rich mesoporous structures represented by NCP and SEP becomes prominent. Compared with macroporous structures which are more readily filled, mesoporous structures often exhibit more outstanding performance in reducing diffusion resistance, increasing adsorption rate and providing greater adsorption capacity.[55] This well explains the better adsorption effect of NCP and SEP compared to RHB when facing most heavy metals.

What's more, although the macroscopic porosity slightly decreased by 1.49–1.78% due to the filling effect of nano-$Al_2O_3$ (Fig. 4b), this physical loss is functionally compensated by

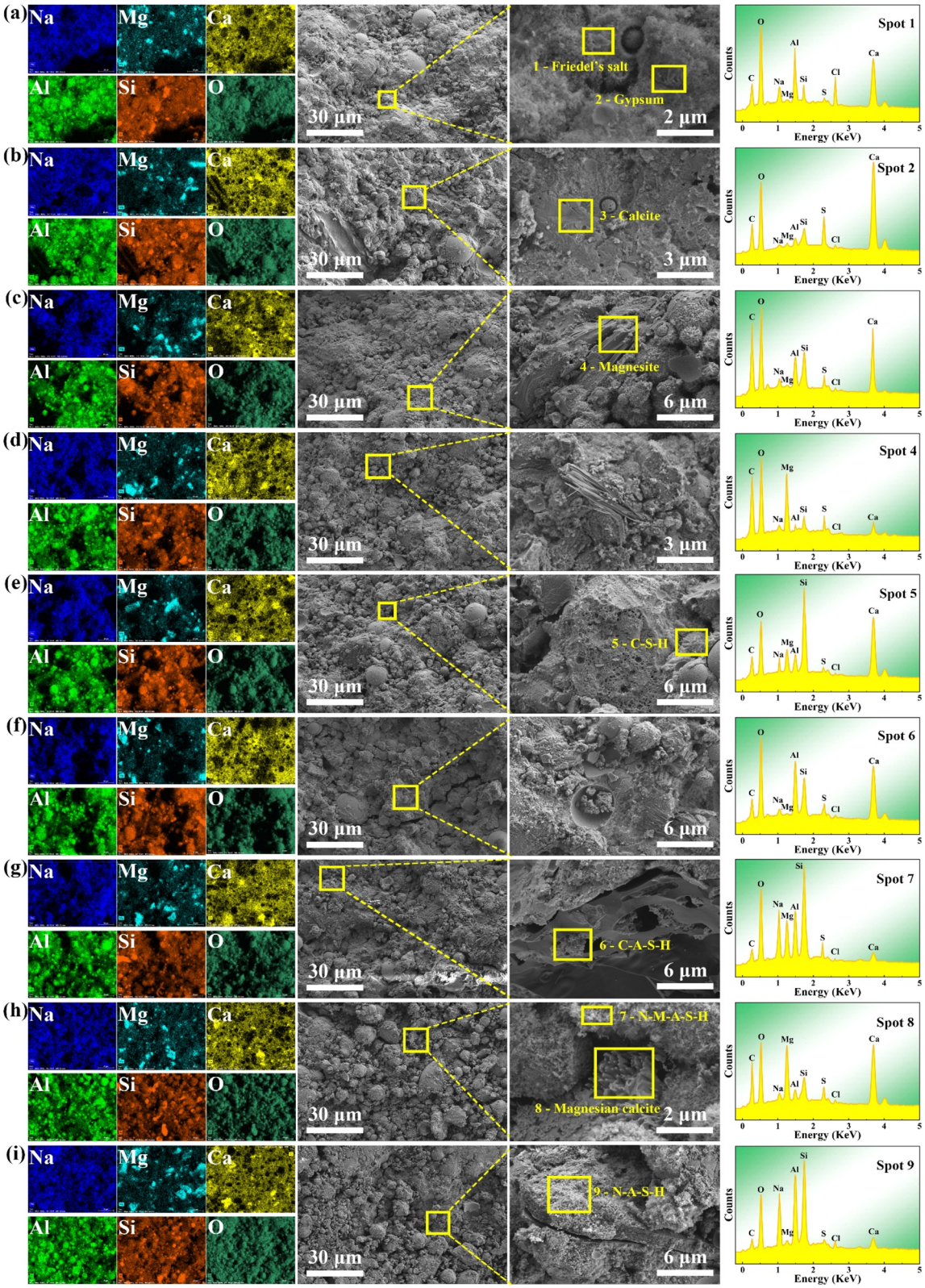


Fig. 7 SEM-EDS images of each group of samples under dry conditions. (a) CCB; (b) CCB-R; (c) CCB-N; (d) CCB-S; (e) CCB-RN; (f) CCB-RS; (g) CCB-Rn; (h) CCB-RNn; (i) CCB-RSn.

chemical enhancement. Specifically, by comparing SEM images in Fig. 8e and b, the introduction of NA further refined the pore structure. EDS surface scans (Fig. 7) also reveal the distribution of Al in the NA-modified groups is more uniform and denser. Moreover, under the influence of Al, the distribution of Na, Mg, Si, Ca, and O also shows this uniform distribution. These

Table 4 Chemical reaction equations of the reaction system

| Reaction type | Reaction equations |
|---|---|
| Hydration reaction | $X\mathrm{Ca^{2+}} + Y[\mathrm{SiO(OH)_3}]^- + \mathrm{H_2O} + (Y - 2X)\mathrm{OH^-} \rightarrow$ C-S-H |
| | $X\mathrm{Ca^{2+}} + Y[\mathrm{Al(OH)_4}]^- + Z[\mathrm{SiO(OH)_3}]^- + \mathrm{H_2O} + (Y + Z - 2X)\mathrm{OH^-} \rightarrow$ C-A-S-H |
| | $X\mathrm{Na^{+}} + Y[\mathrm{Al(OH)_4}]^- + Z[\mathrm{SiO(OH)_3}]^- + \mathrm{H_2O} + (Y + Z - X)\mathrm{OH^-} \rightarrow$ N-M-A-S-H |
| | $X\mathrm{Na^{+}} + Y\mathrm{Mg^{2+}} + Z[\mathrm{Al(OH)_4}]^- + W[\mathrm{SiO(OH)_3}]^- + \mathrm{H_2O} + (Z + W - X - 2Y)\mathrm{OH^-} \rightarrow$ N-M-A-S-H |
| Carbonation reaction | $\mathrm{Ca^{2+}} + 2\mathrm{OH^-} + \mathrm{CO_2} \rightarrow \mathrm{CaCO_3} + \mathrm{H_2O}$ |
| | $\mathrm{Mg^{2+}} + 2\mathrm{OH^-} + \mathrm{CO_2} \rightarrow \mathrm{MgCO_3} + \mathrm{H_2O}$ |
| Reaction under high-salinity conditions | $\mathrm{Ca^{2+}} + \mathrm{SO_4^{2-}} + 2\mathrm{H_2O} \rightarrow \mathrm{CaSO_4 \cdot 2H_2O}$ |
| | $2[\mathrm{Al(OH)_4}]^- + 4\mathrm{Ca^{2+}} + 2\mathrm{Cl^-} + 4\mathrm{H_2O} + 4\mathrm{OH^-} \rightarrow 3\mathrm{CaO \cdot Al_2O_3 \cdot CaCl_2 \cdot 10H_2O}$ |

observations quantitatively indicate that NA acts as effective nucleation sites, facilitating the continuous formation and homogenization of abundant hydration gels (*e.g.*, C-A-S-H). Consistently, TCLP results confirmed that NA addition does not diminish overall heavy metals adsorption. The increase of these active gel phases provides abundant negatively charged sites, which further contribute to heavy metals adsorption *via* electrostatic attraction.[56] Crucially, as corroborated by the FTIR spectra, this gel proliferation also introduces a massive number of oxygen-containing functional groups (*e.g.*, hydroxyls and silanols) that act as robust chemical complexation sites. Together, these chemical enhancements effectively resolving the apparent paradox between the reduced total porosity and the sustained adsorption capacity.

### 3.4. Synergistic mechanisms for controlling heavy metal leaching

Under the continuous influence of high-salinity mine water ions, chemical reactions occur within the filling body, resulting in the formation of various reaction products, with gypsum as a representative phase. During gypsum nucleation and crystallization, its intrinsic expansive properties may induce cracking of the sample upon prolonged exposure to $SO_4^{2-}$. This cracking increases the contact area between the sample and high-salinity mine water, thereby enhancing the leaching concentration of heavy metals such as Mn, Cr, and Ni. Moreover, cations such as $Na^+$, present at the highest concentration, actively participate in cations exchange processes by replacing $Ca^{2+}$ in the gel system. This substitution weakens the cementation ability of the gel, further promoting heavy metals leaching.[52] Fig. 9 reveals the mechanism behind the enhanced leaching of heavy metals under high-salinity conditions.

Under normal conditions, the CCB can initially achieve the immobilization of heavy metals through $CO_2$ sequestration and the formation of gels. SEM results indicate that this immobilization is primarily achieved through the physical "encapsulation" effect, where a substantial amount of gels and carbonates enclose the heavy metals within the matrix. However, other characterization results, such as XRD and FTIR, further demonstrate that these materials also exert a "re-adsorption" effect on the leached heavy metals through chemical pathways. On the one hand, under continuous high-salinity water immersion conditions, some leached heavy metals react with $OH^-$, $SO_4^{2-}$, or $CO_3^{2-}$ introduced into the system,[14] forming insoluble precipitates (such as $Cr(OH)_3$, $PbCO_3$, *etc.*) (eqn (7)–(9)). Notably, the actual solubility of these heavy metal precipitates encompasses not only simple ionic dissolution but also the dissolution of various mononuclear and polynuclear hydroxyl complexes as well as neutral molecules.[57,58] Since these dissolution modes exhibit different dependencies on the solution pH, the alkaline environment established at varying pH levels, influenced by the CCB hydration process, exerts a crucial impact on the solubility of these heavy metal precipitates. Simultaneously, various gels produced in the reaction system form negatively charged Si–$O^-$ groups under alkaline conditions, which can physically attract positively charged heavy metals through electrostatic attraction. Furthermore, metal cations carried by the gels can undergo ions exchange with heavy metals (eqn (10)).[59]

However, the TCLP results indicate that relying solely on the above mechanisms is still insufficient for effective immobilization of heavy metals. The introduction of modifiers for synergistic modification significantly enhances the overall immobilization effect. As shown by XRD and SEM results, the introduction of modifiers, with their abundant pore structures and larger specific surface areas, further increases $CO_2$ adsorption and gel formation.[60] The aforementioned processes—precipitation, ions exchange, and electrostatic attraction—are all effectively enhanced. Additionally, FTIR results show that the introduction of modifiers also brings a variety of functional group structures, such as –OH and –COOH. These surfaces generally carry negative charges, and such negatively charged functional groups (–$COO^-$, –$O^-$) can effectively adsorb cationic heavy metals like $Cr^{3+}$ and $Ni^{2+}$. Moreover, the functional groups exhibit strong complexation capabilities with heavy metals in the solution, forming stable chemical bonds through oxygen-containing functional groups on the surface (eqn (11) and (12)). Among them, RHB (rich in carboxyl and hydroxyl groups) shows a significant effect, while the introduction of NCP and SEP also increases the hydroxyl content of the structure, enhancing the surface complexation potential.

$$n\mathrm{OH^-} + \mathrm{M}^{n+} \rightarrow \mathrm{M(OH)}_n\downarrow \quad (7)$$

$$n\mathrm{SO_4^{2-}} + 2\mathrm{M}^{n+} \rightarrow n\mathrm{M_2SO_4}\downarrow \quad (8)$$

$$n\mathrm{CO_3^{2-}} + 2\mathrm{M}^{n+} \rightarrow n\mathrm{M_2CO_3}\downarrow \quad (9)$$

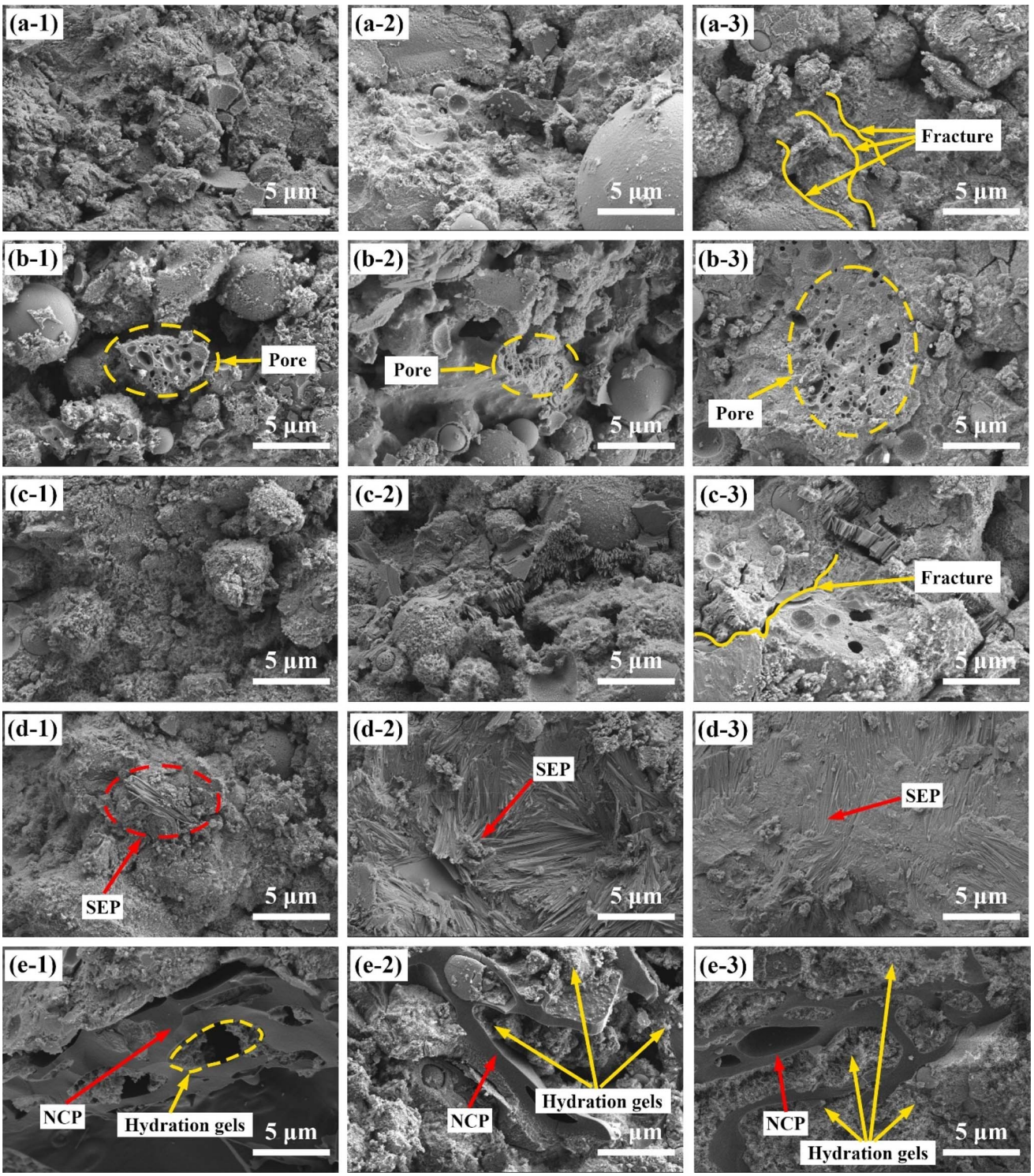


Fig. 8 Microstructure evolution of samples with soaking duration. (a) CCB; (b) CCB-R; (c) CCB-N; (d) CCB-S; (e) CCB-Rn; (1) dried; (2) Immer-3; (3) Immer-60.

$$R - A^{m+} + M^{n+} \rightleftharpoons R - M^{n+} + A^{m+} \quad (10)$$

$$n\text{R–OH} + M^{n+} \rightarrow [(\text{R–O})_n\text{M}] + nH^{+} \quad (11)$$

$$n\text{R–COOH} + M^{n+} \rightarrow [(\text{R–COO})_n\text{M}] + nH^{+} \quad (12)$$

In addition to the above mechanisms, the study have also found that the high-salinity environment rich in $Mg^{2+}$ and $Cl^{-}$ promotes the formation of layered double hydroxides (LDHs) such as meixnerite and Friedel's salt. These LDHs feature bilayer metal hydroxide frameworks composed of divalent

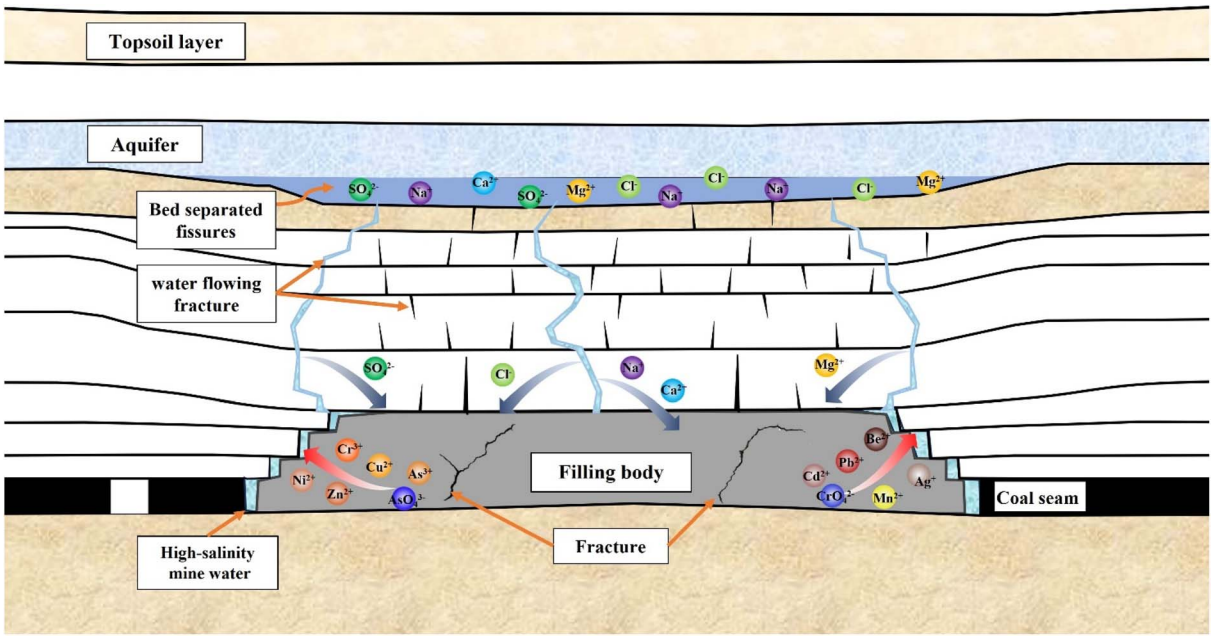


Fig. 9 Heavy metals leaching mechanism of the filling body under high-salinity conditions.

and trivalent cations (*e.g.*, $Mg^{2+}$ and $Al^{3+}$ in meixnerite; $Ca^{2+}$ and $Al^{3+}$ in Friedel's salt), with interlayer anions ($OH^-$ or $Cl^-$) and water molecules, all stabilized by ionic and hydrogen bonds. LDHs structures exhibit excellent adsorption properties arising from their unique physicochemical characteristics.[61] Generally, both exchangeable cations and anions within LDHs are capable of participating in ions exchange actively. Therefore, the heavy metal cations can replace the cations (such as $Mg^{2+}$, $Al^{3+}$, and $Ca^{2+}$, $Al^{3+}$) within the LDH framework. For elements with multiple valence states like Cr, its exact form in the solution—whether Cr(III) or Cr(VI)—dictates its potential immobilization pathway. Any present Cr(III) would be favored to precipitate as hydroxides due to the highly alkaline nature of the CCB, whereas the formation of LDHs provides a mechanistically plausible structural pathway for capturing anionic Cr(VI) species (such as $CrO_4^{2-}$) *via* interlayer anion exchange. Additionally, the interlayer anions can also precipitate and complex with heavy metals. The heavy metals control mechanism of modified filling materials in high-salinity environment is illustrated in Fig. 10.

Overall, within the modified $CO_2$-carbonated cementitious backfill system, the immobilization of heavy metals involves both the physical "encapsulation" and the "re-adsorption" of leached heavy metals, forming a dynamic "release-and-readsorption" equilibrium process. Based on the synergistic effect of these multiple mechanisms, the modified CCB, with its unique structure, demonstrates excellent adsorption performance and can effectively suppress the leaching of heavy metals.

# 4. Discussions

## 4.1. Evaluation of heavy metals immobilization effect

To further contextualize the effectiveness of the proposed synergistic modification system, SI Table S6 presents the percentage reduction in heavy metal leaching for each modified group compared to the unmodified CCB. Meanwhile, SI Table S7 presents a quantitative comparison of heavy metal immobilization performance between the other representative methods published recently. It is worth noting that while biochar, clay minerals (like sepiolite) and nanomaterials have been extensively utilized in soil remediation and wastewater treatment, their specific application for heavy metal control in solid waste backfill, particularly the $CO_2$-carbonated solid waste backfills under high-salinity conditions, remains a largely unexplored domain. As shown in Table S7, traditional methods in soil or water treatment typically achieve removal or immobilization efficiencies ranging from 21% to nearly 100%, or exhibit specific adsorption capacities (*e.g.*, 12.23–833.33 mg $g^{-1}$) depending on the material dosage and target environment. In comparison, despite the harsh, continuous high-salinity immersion in our study—a condition that typically exacerbates heavy metal leaching *via* ion exchange and expansive cracking—our modified CCB system exhibits a better immobilization capability. The synergistic modification method ensures that all the tested heavy metals are controlled within the IV-GQS limit, achieving reduction efficiencies that parallel to those of traditional soil/water treatments (*e.g.*, maintaining 80% to over 95% reduction for key toxic elements like Cr, Ag, and Be in synergistic groups). The results not only highlight the adsorption capacity of the modifiers but also demonstrate the potential of this biochar-clay-nanomaterial synergistic modification strategy in complex, high-salinity underground engineering environments.

Furthermore, when evaluating these reduction efficiencies, it is important to emphasize that the rates currently measured for the biochar-modified groups (*e.g.*, CCB-R) actually represent a conservative estimate. Owing to the trace heavy metals inherently present in the raw biochar, its true immobilization

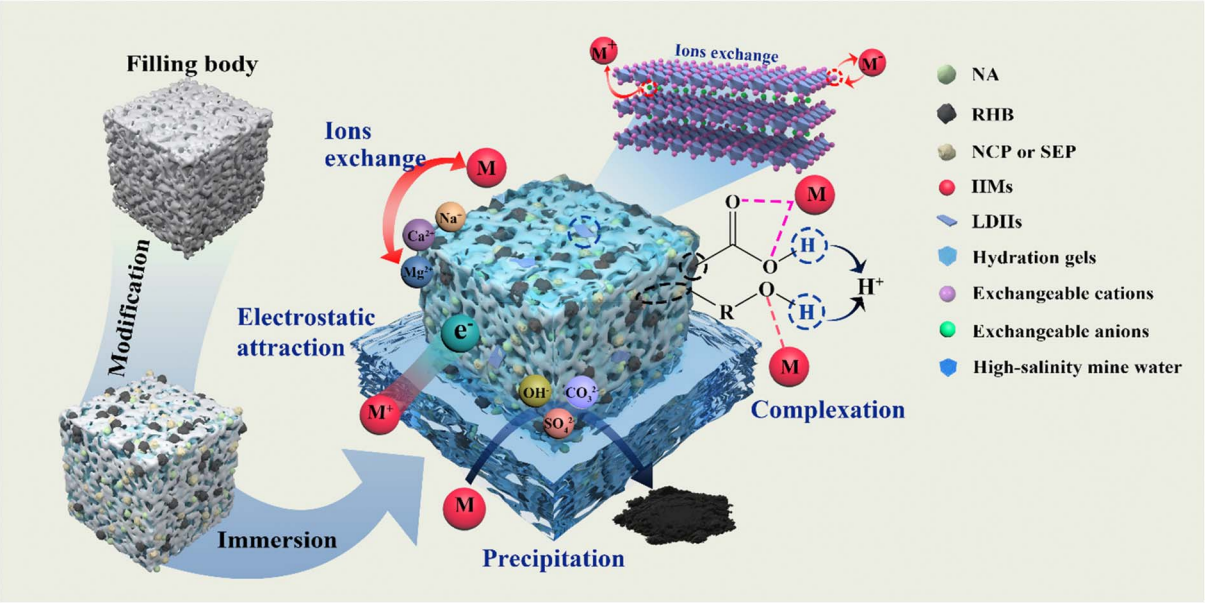


Fig. 10 Synergistic control mechanisms of heavy metals leaching.

efficacy is likely even higher. As evidenced by the experimental results, even within the RHB-inclusive CCB-R group, a substantial decrease in the leaching of heavy metals (with the exception of As) was still observed—for instance, a 77.11% reduction for Cr and a 96.71% reduction for Ag. These findings provide sufficient qualitative evidence that biochar effectively mitigates pollutant leaching from $CO_2$ carbonated coal-based solid waste backfill in high-salinity environments. However, the inevitable presence of inherent heavy metals in biochar poses a methodological challenge. Achieving an accurate quantitative assessment of its pure immobilization capacity without compromising its critical physicochemical properties (*e.g.*, oxygen-containing functional groups) remains a key issue to be addressed in our future research.

### 4.2. Limitations and future work

While the 60 d static leaching test in this study provides some insights into the short-to medium-term physical durability and heavy metals immobilization behavior of the modified CCB, it has certain limitations regarding long-term ecological risk assessment. In actual underground backfill applications, the backfill is subjected to continuous and dynamic high-salinity groundwater penetration over decades. A static immersion experiment cannot fully simulate these complex hydrodynamic conditions and the consequent long-term geochemical evolution of the hydration products. Therefore, to more accurately simulate environmental exposure, future research should incorporate long-term dynamic leaching tests to assess the release kinetics of heavy metals under continuous flow conditions. Furthermore, coupling these experimental data with geochemical modeling software (*e.g.*, PHREEQC) will be highly recommended to predict the multi-decadal phase transformations and long-term ecological impacts of the synergistic modified CCB in high-salinity environments.

Furthermore, while the TCLP method provides a reliable assessment of the maximum leachable toxicity, it cannot identify the specific chemical speciation of the immobilized heavy metals. To address this, future research could consider employing the Tessier 5-step sequential extraction method to analyze the specific occurrence forms of heavy metals. Alongside this speciation analysis, deeper mechanistic investigations are also required. Although Section 3.4 qualitatively classifies the control mechanisms of the modified CCB into physical "encapsulation" and the "re-adsorption" of leached heavy metals, quantitatively distinguishing the exact contribution of each effect to the overall immobilization efficiency remains highly challenging without isotopic-level evidence. Therefore, future work should consider employing isotopic tracing techniques to determine the specific distribution coefficient ($K_d$) of heavy metal migration, which would allow for a rigorous and quantitative decoupling of the heavy metal migration pathways.

## 5. Conclusions

This study investigated the leaching of heavy metals from $CO_2$ carbonated coal-based solid waste backfill (CCB) in high-salinity mine water environments, with a focus on the synergistic modification effects of rice husk biochar (RHB), natural clinoptilolite (NCP), sepiolite (SEP), and γ-phase nano-$Al_2O_3$ (NA). The leaching behavior and control mechanisms of heavy metals in the modified CCB were elucidated, and the mechanical properties were evaluated to assess its engineering applicability. The main findings are summarized as follows:

(1) Mechanical performance was enhanced by over 50% with SEP due to its fibrous structure, whereas RHB exhibited a concentration-dependent effect: it weakened strength at

3 wt% but slightly improved it at 1.5 wt%. NCP reduced strength owing to its low pozzolanic reactivity, which further declined after 60 d of immersion. NA also contributed to strength improvement.

(2) The leaching of heavy metals from CCB under high-salinity environment is primarily driven by the formation of expansive gypsum under high pore water salinity, which induces micro-cracking and facilitates heavy metals release.

(3) Among single-modifier systems, SEP achieved the most pronounced reduction in heavy metals leaching (by an average of 75.78%), though limitations remained for certain elements such as Cr. Synergistic modification effectively compensated for these deficiencies, lowering all heavy metals concentrations below the IV-GQS (based on TCLP results).

(4) The control of heavy metals leaching by synergistic modifiers was attributed to multiple mechanisms, including physical encapsulation, electrostatic attraction, ions exchange, precipitation, and complexation.

## Author contributions

Zhishang Zhang: data curation, writing – original draft, visualization, methodology, formal analysis. Liqiang Ma: conceptualization, funding acquisition, project administration. Ichhuy Ngo: supervision, resources. Kunpeng Yu: formal analysis. Jiangtao Zhai: formal analysis. Zezhou Guo: visualization, formal analysis. Zhiyang Zhao: validation, investigation. Chengkun Peng: data curation, conceptualization. Ruizhi Yang: investigation, software.

## Conflicts of interest

There are no conflicts to declare.

## Data availability

The data supporting this article have been included in the supplementary information (SI). Supplementary information is available. See DOI: https://doi.org/10.1039/d5ra09892k.

## Acknowledgements

The authors appreciate the Xinjiang Uygur Autonomous Region Key R&D Programme Projects (Grant No. 2023B03009-1) for financial support.

## References

1 E. Kaya, B. Ciza, Ç. Yalçınkaya, B. Felekoğlu, H. Yazıcı and O. Çopuroğlu, A comparative study on the effectiveness of fly ash and blast furnace slag as partial cement substitution in 3D printable concrete, *J. Build. Eng.*, 2025, **108**, 112841.

2 J. Zhang, K. Yang, X. He, X. Zhao, Z. Wei and S. He, Research status of comprehensive utilization of coal-based solid waste (CSW) and key technologies of filling mining in China: A review, *Sci. Total Environ.*, 2024, **926**, 171855.

3 M. Fang, N. Yi, W. Di, T. Wang and Q. Wang, Emission and control of flue gas pollutants in $CO_2$ chemical absorption system – A review, *Int. J. Greenh. Gas Control*, 2020, **93**, 102904.

4 X. Cao, Q. Wang, M. Li, C. Ma and S. Wang, Research progress on strengthening mechanism and industrial application of $CO_2$ mineralization technology for coal electricity solid waste, *Results Eng.*, 2025, **27**, 106593.

5 G. V. P. Bhagath Singh and V. Durga Prasad, Environmental impact of concrete containing high volume fly ash and ground granulated blast furnace slag, *J. Clean. Prod.*, 2024, **448**, 141729.

6 L. Velarde, M. S. Nabavi, E. Escalera, M. Antti and F. Akhtar, Adsorption of heavy metals on natural zeolites: A review, *Chemosphere*, 2023, **328**, 138508.

7 P. Yang, L. Liu, Y. Suo, H. Qu, G. Xie, C. Zhang, S. Deng and Y. Lv, Basic characteristics of magnesium-coal slag solid waste backfill material: Part I. preliminary study on flow, mechanics, hydration and leaching characteristics, *J. Environ. Manage.*, 2023, **329**, 117016.

8 K. Long, B. Li, J. Ma, H. Liu and J. Li, Ecological risk analysis of leakage caused by coal-based solid waste backfill slurry bleeding: An experimental study, *J. Clean. Prod.*, 2025, **494**, 144993.

9 Y. Hu, J. Tang, Y. Fei, J. Shang, P. Liu and Y. Liu, Enhancement of Zn adsorption on coal fly ash-based geopolymer with steel slag incorporation: Leaching behavior and performance insights, *Environ. Pollut.*, 2025, **367**, 125639.

10 J. A. Meima, R. D. van der Weijden, T. T. Eighmy and R. N. J. Comans, Carbonation processes in municipal solid waste incinerator bottom ash and their effect on the leaching of copper and molybdenum, *Appl. Geochem.*, 2002, **17**, 1503–1513.

11 Y. Wang, L. Hu, Y. Zhang and L. Dong, Experimental study on the scaling law of the heat exchange tube surface in the process of low-temperature single-effect distillation of high-mineralized mine water, *Desalination Water Treat.*, 2024, **319**, 100571.

12 Q. Y. Chen, M. Tyrer, C. D. Hills, X. M. Yang and P. Carey, Immobilisation of heavy metal in cement-based solidification/stabilisation: A review, *Waste Manage.*, 2009, **29**, 390–403.

13 L. Chen, K. Nakamura and T. Hama, Review on stabilization/solidification methods and mechanism of heavy metals based on OPC-based binders, *J. Environ. Manage.*, 2023, **332**, 117362.

14 B. Guo, B. Liu, J. Yang and S. Zhang, The mechanisms of heavy metal immobilization by cementitious material treatments and thermal treatments: A review, *J. Environ. Manage.*, 2017, **193**, 410–422.

15 K. Polipalli, S. Suraboyina, M. Kashimalla and A. Polumati, A review on value addition of Agricultural Residues by Chemical and Bio-chemical Processes to abate environmental pollution, *Green Technol. Sustainability*, 2025, **3**, 100241.

16 R. Hou, B. Zhu, L. Wang, S. Gao, R. Wang and D. Hou, Mechanism of clay mineral modified biochar simultaneously immobilizes heavy metals and reduces soil carbon emissions, *J. Environ. Manage.*, 2024, **361**, 121252.
17 S. S. Senadheera, S. Gupta, H. W. Kua, D. Hou, S. Kim, D. C. W. Tsang and Y. S. Ok, Application of biochar in concrete – A review, *Cem. Concr. Compos.*, 2023, **143**, 105204.
18 W. Liu, S. Tan, L. Qing and Y. Li, Pozzolanic activity of biochar with high carbon content and its influence on comprehensive strength-emission performance of biochar-cement composite paste, *Constr. Build. Mater.*, 2025, **478**, 141427.
19 L. Chen, L. Wang, Y. Zhang, S. Ruan, V. Mechtcherine and D. C. W. Tsang, Roles of biochar in cement-based stabilization/solidification of municipal solid waste incineration fly ash, *Chem. Eng. J.*, 2022, **430**, 132972.
20 I. Khan, H. A. Saddiqi, F. Ahmad and A. Ullah, Mortar performance enhancement by partially replacement of cement with hybrid biochar: An experimental evaluation and machine learning predictions of compressive strength, water absorption and thermal conductivity, *Mater. Chem. Phys. Sustain. Energy*, 2025, **3**, 100024.
21 S. Xie, L. Huang, C. Su, J. Yan, Z. Chen, M. Li, M. Du and H. Zhang, Application of clay minerals as adsorbents for removing heavy metals from the environment, *Green Smart Min. Eng.*, 2024, **1**, 249–261.
22 J. Li, M. Gao, W. Yan and J. Yu, Regulation of the Si/Al ratios and Al distributions of zeolites and their impact on properties, *Chem. Sci.*, 2023, **14**, 1935–1959.
23 K. Gu, M. Zhu, Q. Song and Z. Jiang, Hydration and microstructure formation of magnesium oxysulfate (MOS) cement regulated by sepiolite with high adsorption ability, *Cem. Concr. Compos.*, 2024, **153**, 105728.
24 C. Sánchez-Mendieta, J. J. Galán-Díaz and I. Martinez-Lage, Relationships between density, porosity, compressive strength and permeability in porous concretes: Optimization of properties through control of the water-cement ratio and aggregate type, *J. Build. Eng.*, 2024, **97**, 110858.
25 M. Seifan, S. Mendoza and A. Berenjian, Mechanical properties and durability performance of fly ash based mortar containing nano- and micro-silica additives, *Constr. Build. Mater.*, 2020, **252**, 119121.
26 S. Said, S. Mikhail and M. Riad, Recent processes for the production of alumina nano-particles, *Mater. Sci. Energy Technol.*, 2020, **3**, 344–363.
27 D. Kim, C. Lee, B. G. Lee, J. Park, K. C. Kim, J. K. Choe, P. Westerhoff and H. Rho, $\gamma$-$Al_2O_3$ selectively adsorbs transition group metals from contaminated waters to produce bi-metallic catalysts for efficient nitrate reduction, *J. Hazard. Mater.*, 2025, **493**, 138428.
28 R. Prins, On the structure of $\gamma$-$Al_2O_3$, *J. Catal.*, 2020, **392**, 336–346.
29 AQSIQ and SAC, *Test Method of Cement Mortar Strength (ISO Method)*, 2021.
30 EPA, *Synthetic Precipitation Leaching Procedure*, 1994.
31 AQSIQ and SAC, *Methods for Determining the Uniaxial Compressive Strength and Counting Softening Coefficient*, 2009.
32 AQSIQ and SAC, *Standard for Groundwater Quality*, 2017.
33 Z. Li, Y. Huang, Z. Zhu, H. Shi, Y. Xiao, H. Song, W. Zuo, H. Zhou, S. Wang and L. Dong, Research on the stepwise treatment of phytoremediation residue: Combining leaching pretreatment with pyrolysis, *Process Saf. Environ. Prot.*, 2025, **194**, 74–82.
34 Z. A. AlDhawi, I. I. BinSharfan and M. A. Abdulhamid, Carboxyl-functionalized polyimides for efficient bisphenol A removal: Influence of wettability and porosity on adsorption capacity, *Chemosphere*, 2023, **313**, 137347.
35 I. Ngo, L. Ma, J. Zhai, Y. Wang and T. Wei, Durability of $CO_2$-fly ash-based backfill materials in cation water deterioration, *Int. J. Min. Reclamat. Environ.*, 2023, **37**, 544–567.
36 C. Cai, F. Li, S. Fan, D. Yan, Q. Sun, H. Jin, J. Shao, Z. Chen and M. Liu, Investigation on deterioration mechanism of geopolymer cemented coal Gangue-Fly ash backfill under combined action of high temperature and salt corrosion environment, *Constr. Build. Mater.*, 2023, **398**, 132518.
37 L. Qing, H. Zhang and Z. Zhang, Effect of biochar on compressive strength and fracture performance of concrete, *J. Build. Eng.*, 2023, **78**, 107587.
38 M. S. Islam, B. J. Mohr and D. VandenBerge, Performance of natural clinoptilolite zeolite in the cementitious materials: A comparative study with metakaolin, fly ash, and blast furnace slag, *J. Build. Eng.*, 2022, **53**, 104535.
39 D. Salehzadeh, B. Elahi, J. E. Ten Elshof, G. Brem and M. Mehrali, Synergistic effect of sepiolite as an active binder for enhancing mechanical stability of porous $K_2CO_3$ granules in thermochemical heat storage, *Chem. Eng. J. Adv.*, 2025, **23**, 100783.
40 K. Sargunan, M. Venkata Rao, A. Alex Rajesh, R. Babu, P. Prasanthni, K. Jagadeep and M. L. Rinawa, Experimental investigations on mechanical strength of concrete using nano-alumina and nano-clay, *Mater. Today: Proc.*, 2022, **62**, 5420–5426.
41 Z. Zhang, L. Ma, I. Ngo, C. Peng, J. Zhai and Z. Guo, Effect of Mine Water Environment on Durability of Solid Backfilling Based on Carbonated Coal-Based Waste, *ACS Omega*, 2025, **10**, 17626–17641.
42 W. Wang, B. Wang and S. Zhang, Dispersion, properties, and mechanisms of nanotechnology-modified alkali-activated materials: A review, *Renewable Sustainable Energy Rev.*, 2024, **192**, 114215.
43 Z. X. Chen, N. T. Zhang and S. H. Chu, Role of alkalinity in $CO_2$ sequestration of $\gamma$-belite, *Constr. Build. Mater.*, 2024, **432**, 136508.
44 O. Yazici and S. Yilmaz, Production and characterisation of LDH meixnerite powders, *Adv. Appl. Ceram.*, 2010, **109**, 341–345.
45 Y. Guan, Y. Xia, L. Chen, B. Guo and L. Wang, Efficient adsorption of heavy metals using Friedel's salt synthesized from municipal solid waste incineration fly ash leachate, *Environ. Res.*, 2025, **285**, 122330.
46 T. Hou, L. Yan, S. Yang, J. Li, X. Li and Y. Zhao, Efficient removal of graphene oxide by $Fe_3O_4$/MgAl-layered double

hydroxide and oxide from aqueous solution, *J. Mol. Liq.*, 2019, **284**, 300–306.
47 S. Liu, C. Zhang, C. Hu, K. Mei and X. Cheng, Study on low thermal conductivity cement reinforced by sepiolite fiber for deep geothermal well, *Geothermics*, 2025, **129**, 103290.
48 I. Ngo, L. Ma, J. Zhai, Y. Wang, Y. Xu, T. Wei and K. Yu, Effect of the co-activation of sodium silicate and $CO_2$ on setting and mechanical properties of coal gangue-fly ash backfill (CGFB), *Environ. Earth Sci.*, 2023, **82**, 190.
49 D. Liang, F. Wang, S. Xue, J. Yan, Y. Xu, G. Lv and J. Yan, Purification of waste liquids from alkaline washing pretreatment of municipal solid waste incineration fly ash using Friedel's salt, *J. Environ. Manage.*, 2025, **380**, 125020.
50 U. A. Birnin-Yauri and F. P. Glasser, Friedel's salt, $Ca_2Al(OH)_6(Cl,OH)\cdot 2H_2O$: its solid solutions and their role in chloride binding, *Cem. Concr. Res.*, 1998, **28**, 1713–1723.
51 S. Fan, M. Zhao, J. Luo, W. Li, X. Fan, N. Zhou, H. Xu and Y. Shi, Facile preparation of N/P co-doped mesoporous biochar for efficient removal of methylene blue from aqueous solutions: A 2D-FTIR-COS, adsorption mechanism analysis, and fixed-bed column study, *J. Water Process Eng.*, 2025, **72**, 107479.
52 Y. Wang, Y. Cao, Z. Zhang, P. Zhang, Y. Ma, A. Wang and H. Wang, Intrinsic sulfuric acid resistance of C-(N)-A-S-H and N-A-S-H gels produced by alkali-activation of synthetic calcium aluminosilicate precursors, *Cem. Concr. Res.*, 2023, **165**, 107068.
53 M. Cantaluppi, V. Diella, A. Pavese, M. Marchi and N. Marinoni, Crystallisation and phase transformation processes during clinkering in portland cement (pc) by means of *in situ* and *ex situ* analyses, *Constr. Build. Mater.*, 2023, **394**, 132261.
54 Q. Dong, B. Liang, L. Jia and L. Jiang, Effect of sulfide on the long-term strength of lead-zinc tailings cemented paste backfill, *Constr. Build. Mater.*, 2019, **200**, 436–446.
55 Y. Mei, S. Zhuang and J. Wang, Adsorption of heavy metals by biochar in aqueous solution: A review, *Sci. Total Environ.*, 2025, **968**, 178898.
56 N. Gineys, G. Aouad and D. Damidot, Managing trace elements in Portland cement – Part I: Interactions between cement paste and heavy metals added during mixing as soluble salts, *Cem. Concr. Compos.*, 2010, **32**, 563–570.
57 Y. F. Orlov, E. I. Maslov and E. I. Belkina, Solubilities of metal hydroxides, *Russ. J. Inorg. Chem.*, 2013, **58**, 1306–1314.
58 F. Scholz and H. Kahlert, The calculation of the solubility of metal hydroxides, oxide-hydroxides, and oxides, and their visualisation in logarithmic diagrams, *ChemTexts*, 2015, **1**, 7.
59 M. L. D. Gougar, B. E. Scheetz and D. M. Roy, Ettringite and C-S-H Portland cement phases for waste ion immobilization: A review, *Waste Manage.*, 1996, **16**, 295–303.
60 T. Wang, X. Quan, Z. Sun and Z. Sun, Sustainable biochar synthesis *via* synergistic $H_2O_2$-KOH modification for enhanced $CO_2$ physisorption, *Carbon Capture Sci. Technol.*, 2025, **15**, 100438.
61 L. Chi, C. Huang, Z. Li, S. Ruan, B. Peng, M. Li, Q. Liang, K. Yin and S. Lu, Heavy metals immobilization of LDH@biochar-containing cementitious materials: Effectiveness and mechanisms, *Cem. Concr. Compos.*, 2024, **152**, 105667.